Design Description Document

Nanostructured MIR Optical Filters

Team: Peter Fiala, Guntis Rutins, Andrew Kruse, Ty Adair

Customer: Mike Tatarak, Materion

Advisors: Brian McIntyre, Nick Vamivakas, Jim Mitchell

Document Number 01

Revisions Level	Date
G	27 April 2016

Rev	Description	Date	Authorization
A	Initial Document	01 February 2016	AK
B	First Update	11 February 2016	PF
C	Updated Goals and Progress	25 February 2016	PF
D	Addressing Knox's Comments	27 February 2016	PF
E	Updated Manufacturing and Design	31 March 2016	PF
F	More Manufacturing and Design Updates	19 April 2016	PF
G	Manufacturing Updates and Finalization	27 April 2016	GR

Table of Contents

Vision Statement

The project team shall produce methods for designing and manufacturing nanostructures with optical properties that selectively transmit or reflect certain bandwidths of electromagnetic radiation, relying on the physics of sub-wavelength diffraction.

Project Scope

We are responsible for a design study of long-wavelength pass MIR optical filters. This includes both a design that meets the specifications provided, and an explanation as to what different design factors there are and how they affect filter performance.

It is desirable that we expand this design study to short-wavelength pass, band pass, and band stop filters. It is desirable that we produce a manufacturing plan for proof of concept devices.

We are not responsible for any sort of industrial-scale manufacturing plan, or any devices on a larger scale than necessary for proof of concept.

System Overview

The basic structure of the system is an array of subwavelength scale features. These could be pillars, holes, cones, microlenses, or any combination thereof. The arrays should be made of only etched silicon. Other materials are acceptable, but discouraged.

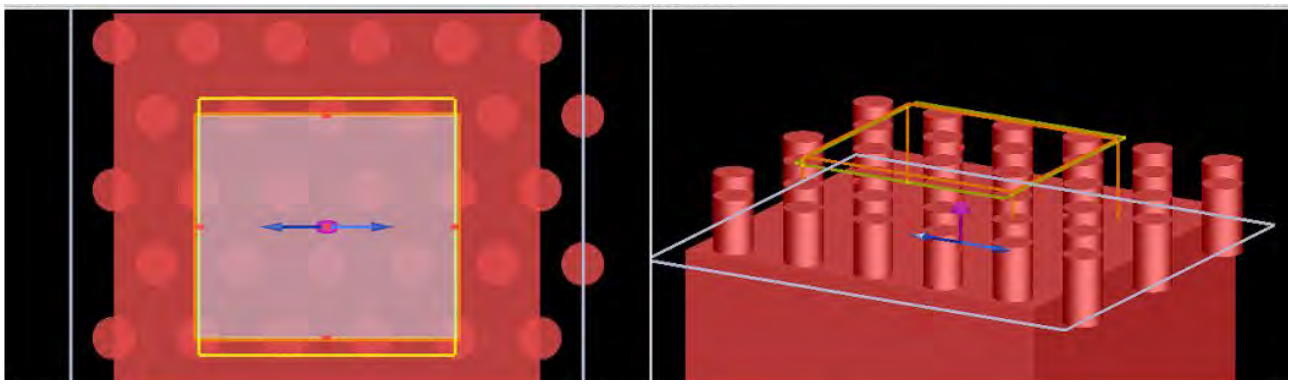

Figure 1: Examples of this type of array modeled in Lumerical FDTD Solutions. This is a simulation of cylinders etched into silicon at a regular hexagonal pattern.

There are various parameters that need to be characterized, including feature size, shape, spacing, distribution, height, and more. The initial design is an array that is manufacturable with the mask that we have, and it will be iterated off of this in order to learn about how these variables affect overall performance.

Devices are to be designed in Lumerical FDTD Solutions (Finite Difference Time Domain), manufactured through various methods in UR Nano, and measured with FTIR interferometer spectroscopy. Eventually, all three branches will come together to design, produce, and measure a proof of concept device.

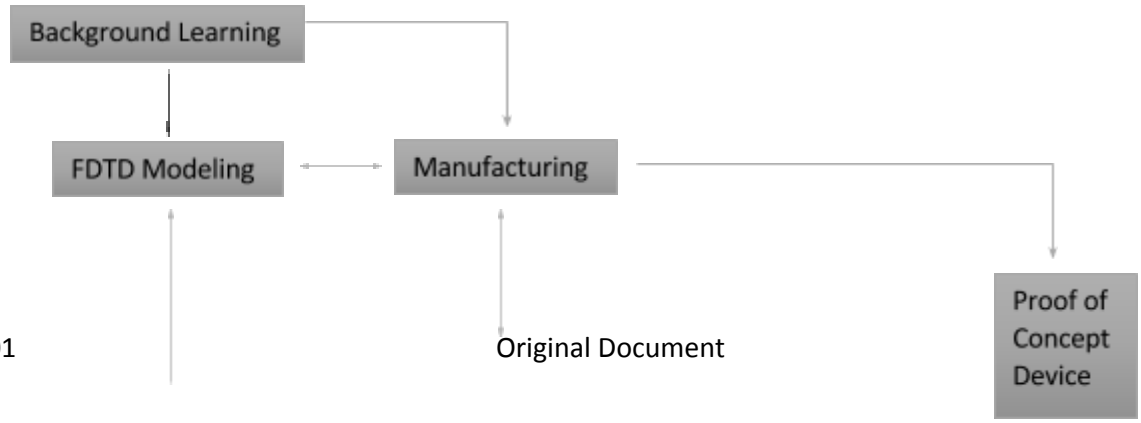

Metrology

Software Calibration

The first thing that we did with the software was to calibrate it to a known spectrum. To do this, we compared simple simulations to mathematical models that we could calculate confidently. We obtained refractive index vs wavelength data from refractiveindex.info and used it to calculate the basic Fresnel reflection and transmission as a function of wavelength. This was then mimicked in Lumerical both with light entering and exiting the medium at an interface with a uniform n=1 material. The materials chosen were silicon and water. Silicon was chosen because it is the material we will use the most, and water because it is one of the only materials in Lumerical's material database that has spectral features in the 1-12µm range. The comparison is shown in figure 2.

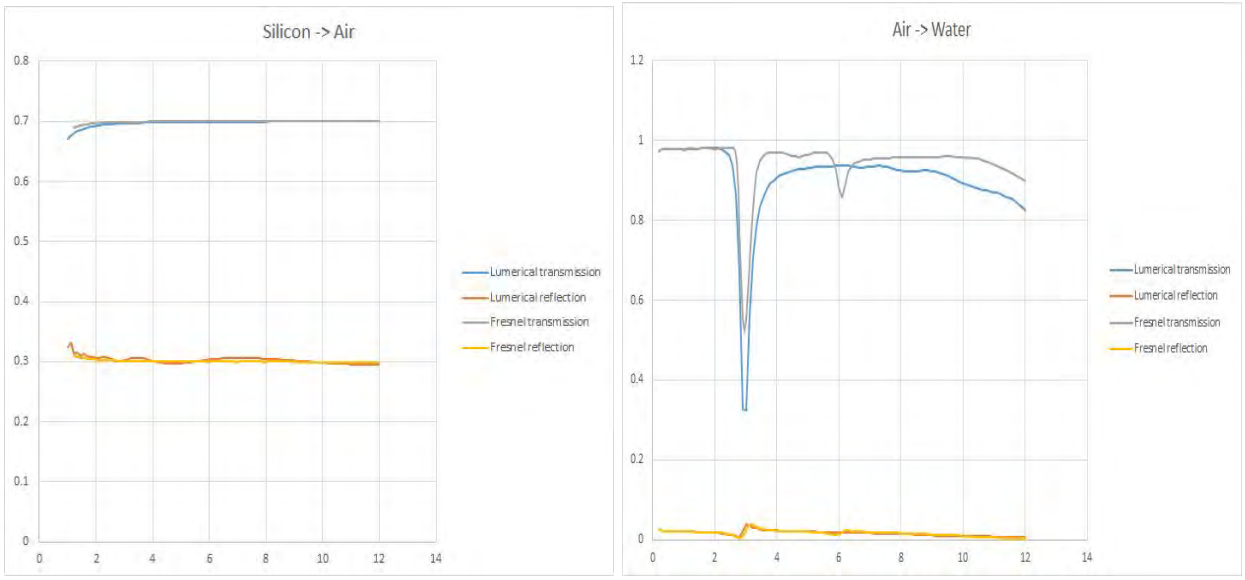

Figure 2: Comparison of calculations done in Lumerical with those done using Fresnel coefficients. For silicon, both transmission and reflection are nearly indistinguishable. For water, reflection is nearly identical. Transmission is similar for most of the spectrum, but Lumerical misses the absorption around 6µm. This isn't particularly worrisome because we will probably only ever use silicon.

Plasmonic Design

After calibration,modeling of actual filters began. The first variable tested was the difference between a square array and a hexagonal array of nano-apertures. After that, aperture spacing will be varied, and the results compared to establish a relationship between this and the spectral features that the customer is interested in.

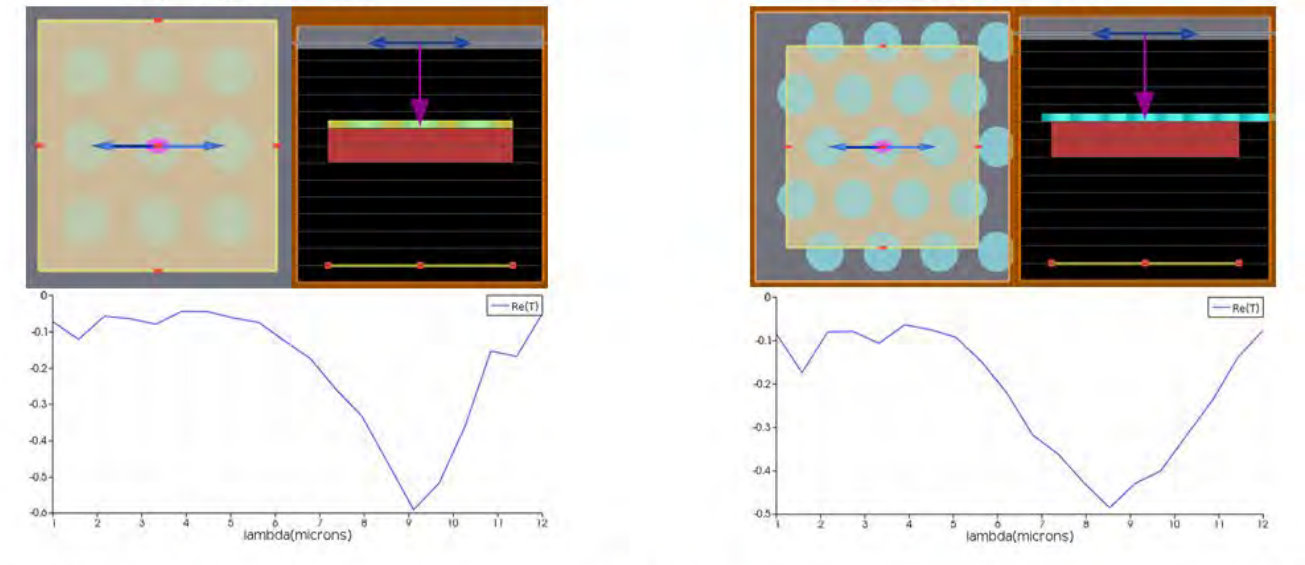

Figure 3: The difference produced by changing the type of array. Both simulations are a 50nm layer of gold on a silicon substrate. Since we are trying to produce a broad area of blocking, this results indicate that a hexagonal array will work better.

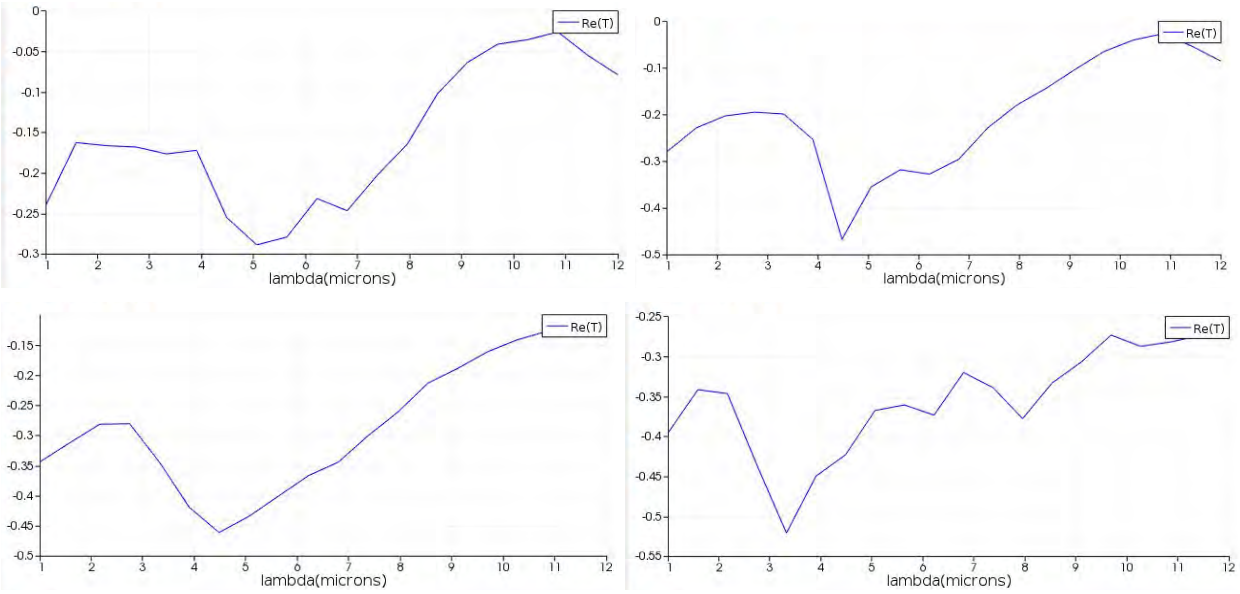

Figure 4: The spectra of nano-aperture arrays as the hole to hole spacing is changed. All of them are made of a 50nm silicon nitride membrane with 50nm of gold on it. The holes go through both layers and are 3µm in diameter. The spacings are 5, 4.5, 4, and 3.5µm, respectively. The minimum transmission point can be seen to follow these values as they decrease.

Obviously, these spectra don't look anything like what the customer wants from a filter, but as more variables are tested, we expect to be able to shape these spectra and make them closer to specifications. All of the above simulations were done with metallic films. After this point, the focus of the designs was shifted to filters that only use silicon. Plasmonic designs haven't been completely abandoned, but our customer has experience with more optimized designs for this type of device. In his experience, full optimization of optical properties results in an incredibly small and fragile device that isn't practical for use.

Etched Silicon Design

The first few things done with silicon design were simple parameter sweeps. This is a built in function of Lumerical that takes a base structure and varies one variable within set ranges. Lumerical then runs the simulations in parallel, which slightly decreases the computation time. The first two successful parameter sweeps separately varied the pillar diameter and height. Results are shown in figures 6-9.

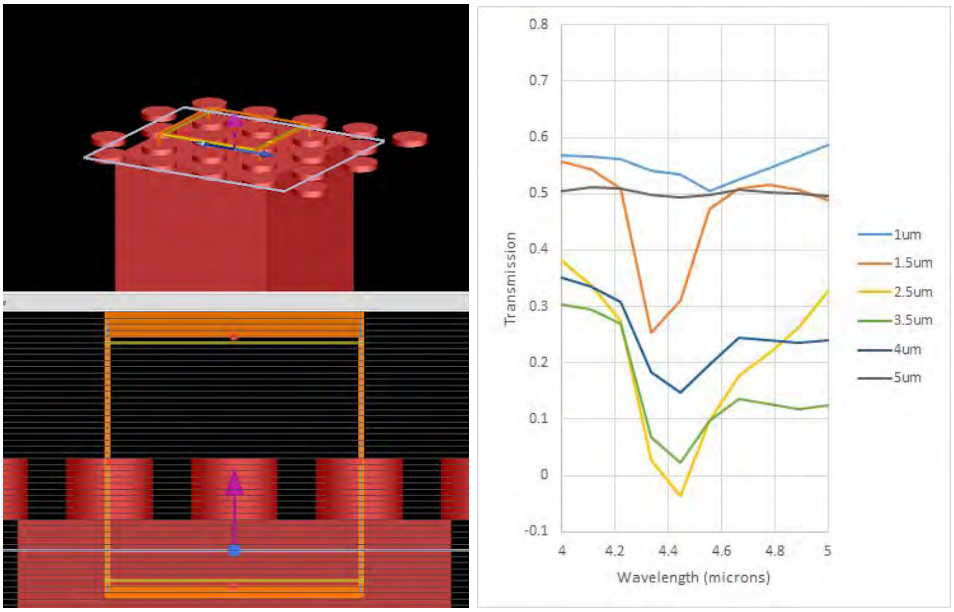

Figure 5: For these data, pillar diameter was varied. Spacing was 5µm hexogonal, height was 1µm, the light exited from the substrate into a uniform n=1 space. On the left is one of the simulations from the sweep (3.0µm). On the right is the part of the spectrum where an effect was observed. The main feature noticed is that a transmission dip appears in every spectrum at the same place, but becomes much more pronounced for certain pillar diameters. This didn't give us the desired spectrum, but it was useful information about how to sharpen spectral features.

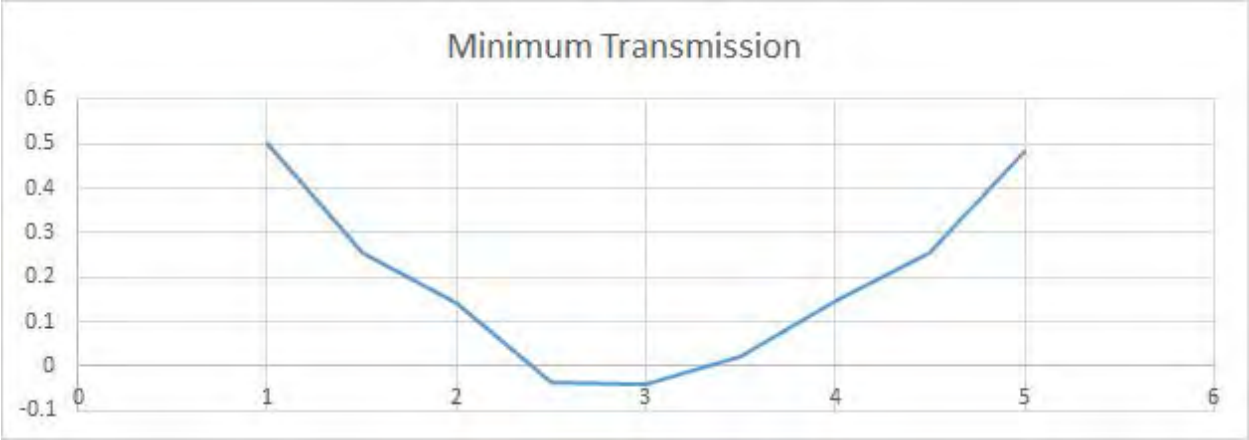

Figure 6: Minimum transmission as a function of pillar diameter from the results above. The negative values are an artifact of running a faster, less accurate simulation. These data show a clear relationship that is the kind of variable our customer wants us to characterize.

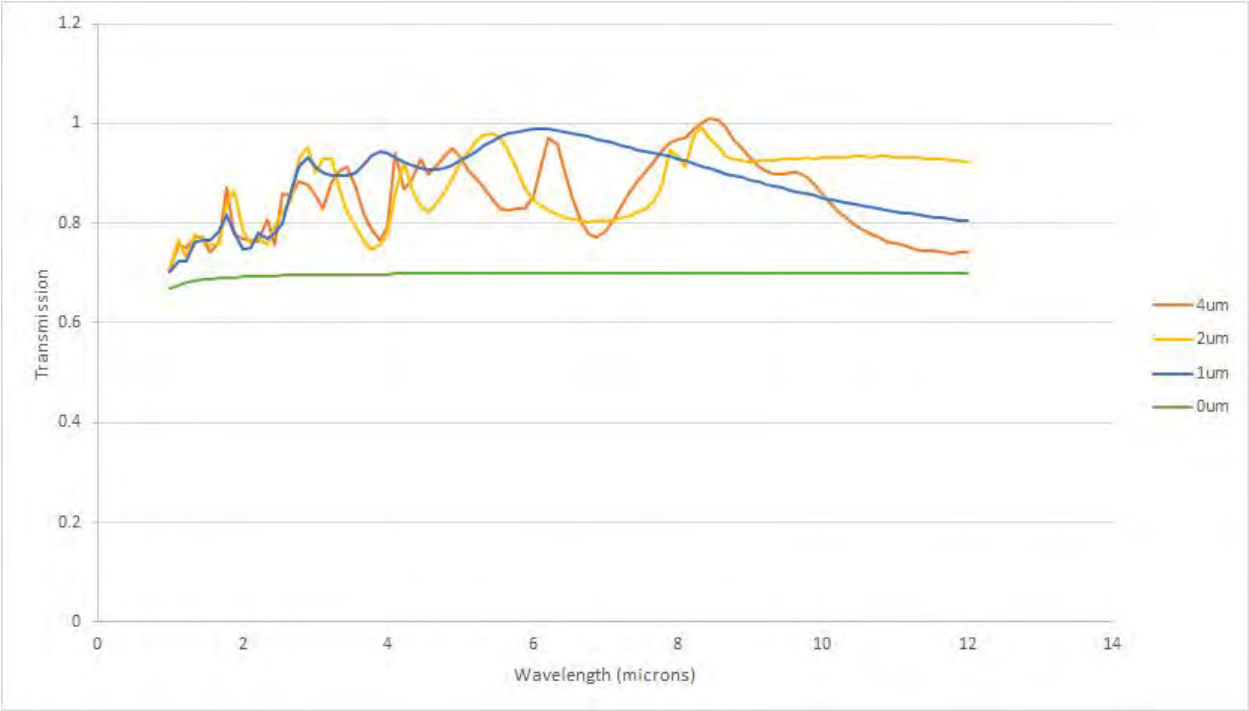

Figure 7: Transmission for various pillar heights. Light going from n=1 space into the substrate, 1.5µm pillar diameter, 3µm hexagonal spacing. The main observation from these data is that taller pillars result in much bumpier spectra. This is likely because longer pillars begin to exceed $\lambda/4$, at which point the layer of pillars may start behaving similarly to thin films.

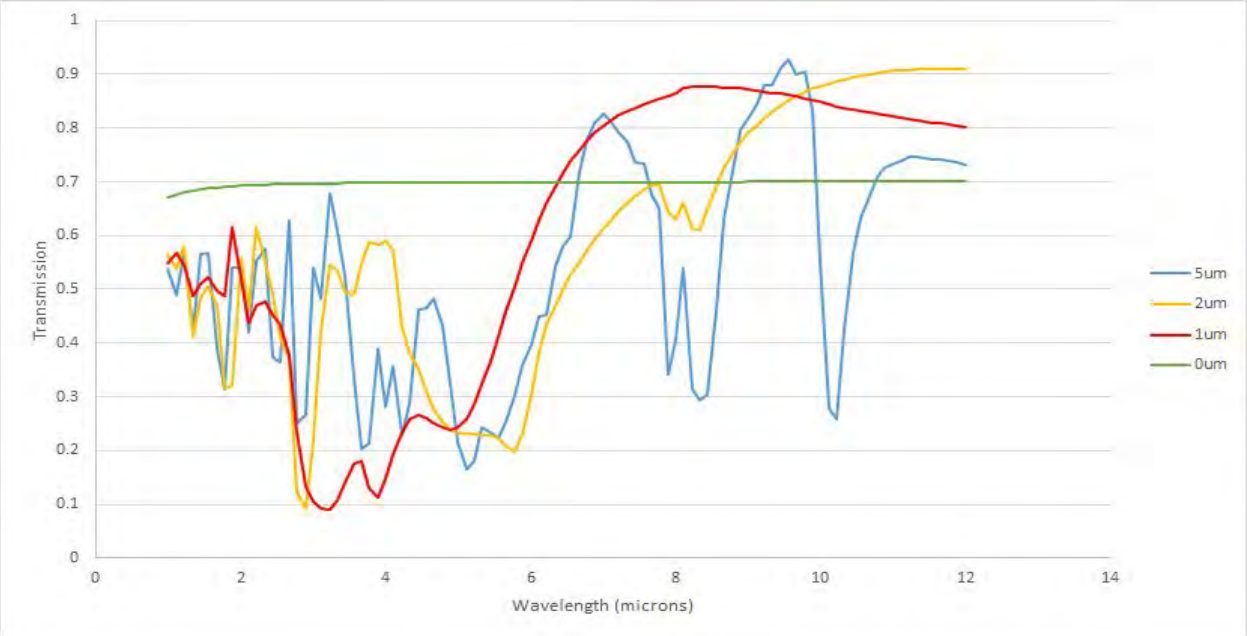

Figure 8: Transmission for the exact same array and sweep as above, but with light leaving the substrate. the same conclusions can be drawn from this, with the addition that light leaving the substrate gives much better extinction for lower wavelengths.

After the cylindrical pillar geometry, the next set of simulations was with hexagonal pyramids. The principle was that these shapes might refract away shorter wavelengths while passing longer wavelengths that are too big to 'see' them. The first two simulations both employed 2µm pyramid diameters, 2µm spacing, and light exiting from the substrate. The results were very encouraging, and are shown in figures 10-12.

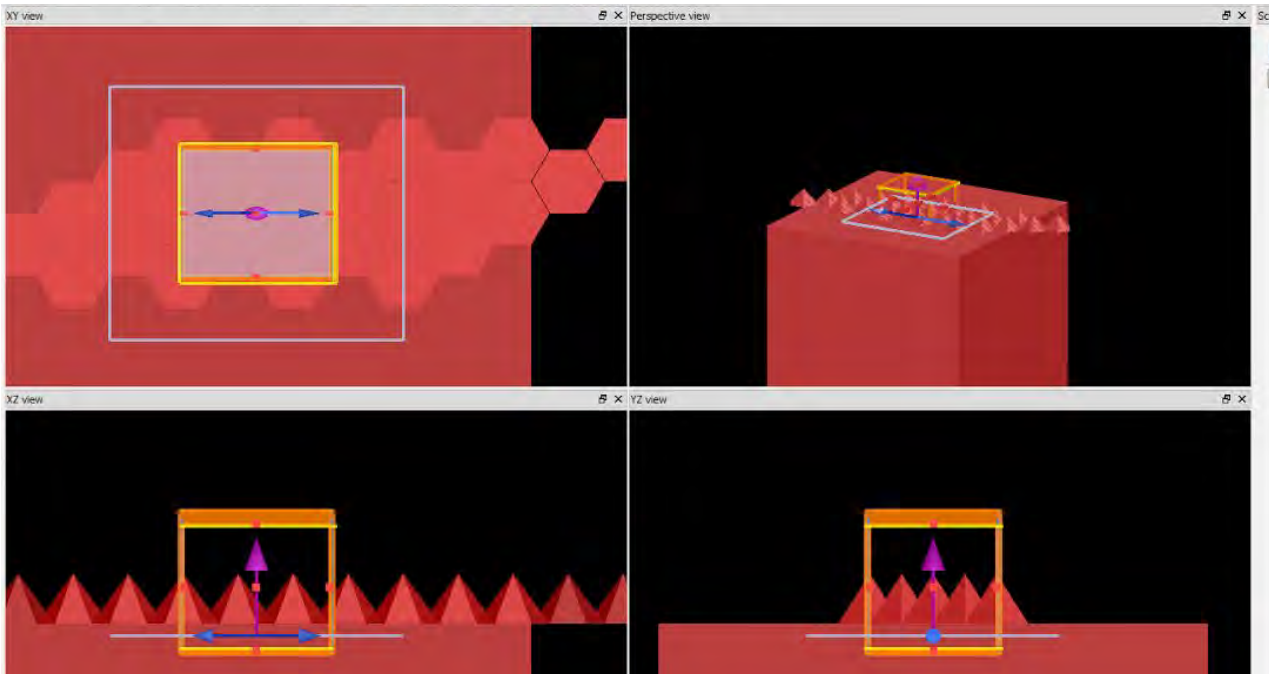

Figure 9: Images of the hexagonal pyramid simulation. Boundaries are chosen so that their boundary conditions will mirror along the array's axes of symmetry.

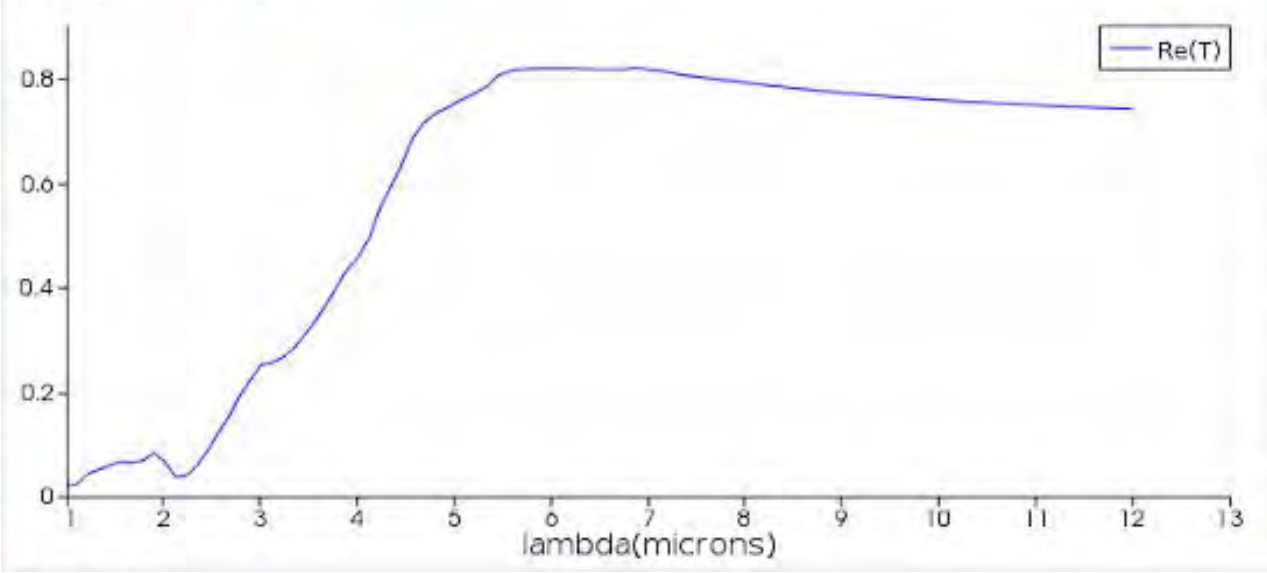

Figure 10: Transmission of 1µm tall hexagonal pyramids. This began to resemble to spectrum we want, so the next step was to iterate and see how each variable affects performance.

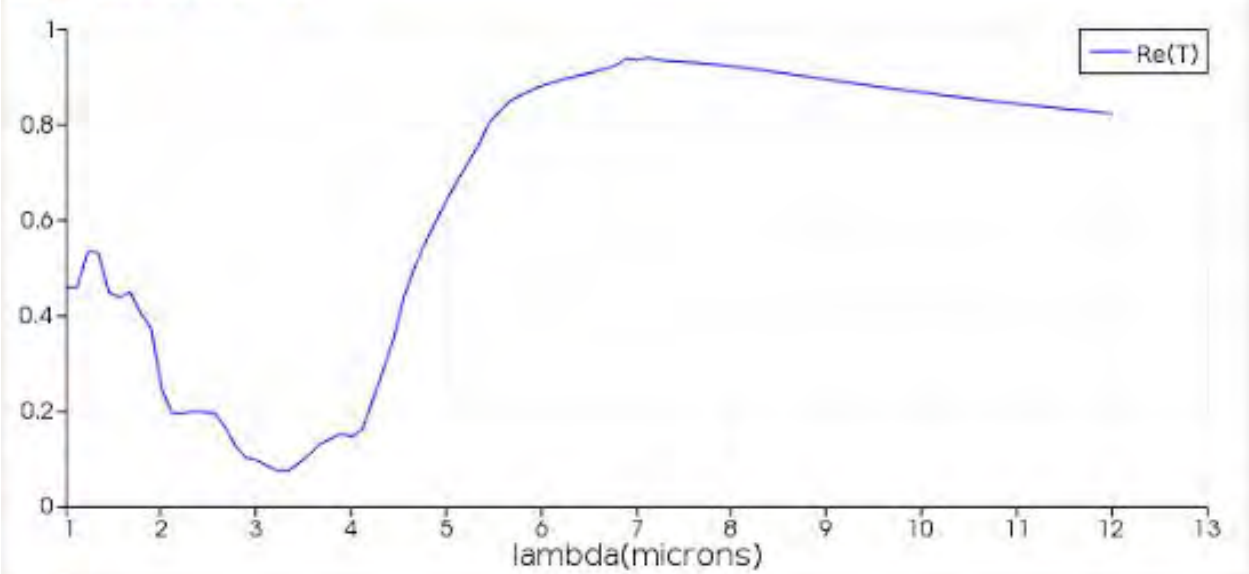

Figure 11: Transmission of 2µm tall hexagonal pyramids. The spectrum shifted to longer wavelengths from that of the the 1µm tall hexagonal pyramids.

Results from hexagonal pyramid arrays were encouraging, however current our available etching methods were insufficient to produce the precision necessary for manufacturing without significant and costly production time. Due to this issue, we switched to a more simple design that requires less strict etching methods: right circular cones. After many parameter sweeps, different variables were isolated and their effects on performance.

As a general designing guide, there are 2 degrees of freedom of this geometry that beneficially affect the design's theoretical transmission spectrum. These parameters are cone height and base diameter. First, the diameter of the base of the cones controls the cutoff wavelength where the transmission rises over a few microns to a value above the normal transmission of bare silicon. The peak wavelength is reliably around 3x the base diameter of the cones. As the height of cones is varied, the peak wavelength whereafter the transmission begins to drop remains constant if the base diameter is constant. The height of the cones can control the slope during transition from stopband to bandpass, but affects the quality of the stopband.

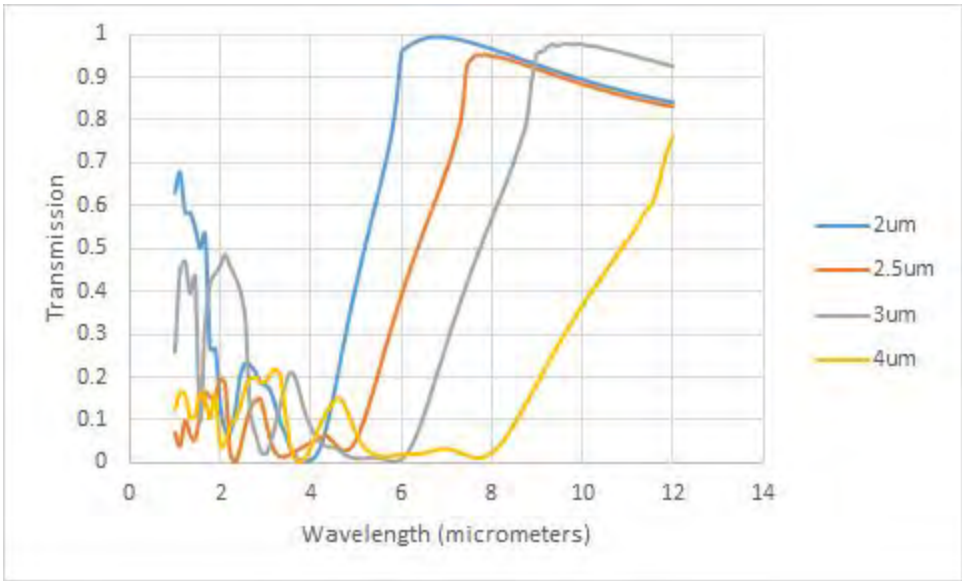

Figure 12: Cutoff wavelength for cones with varying base diameter. Diameters are given in the legend. The wavelength where the transmission initially drops off is roughly three times the diameter.

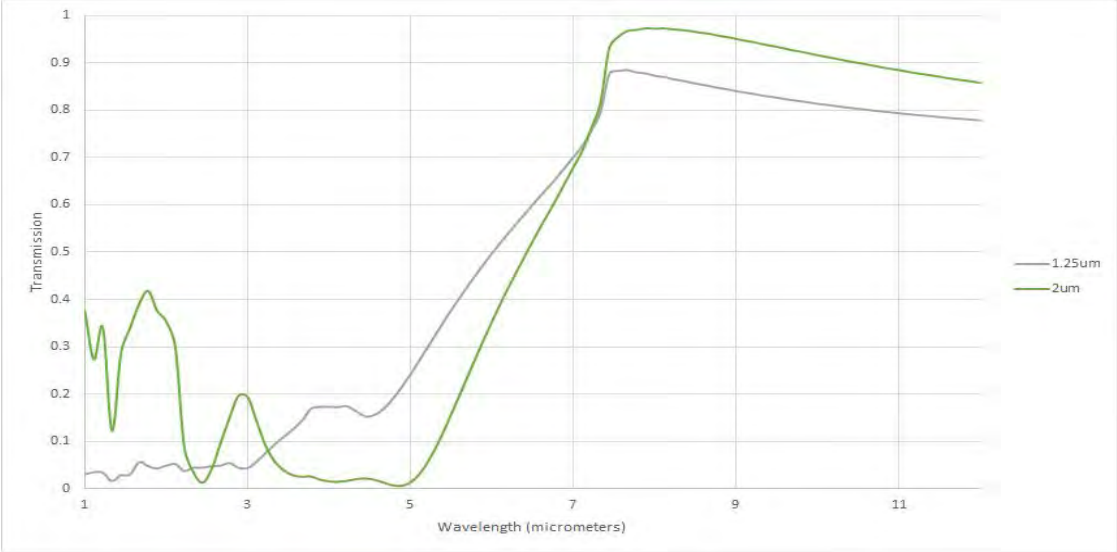

Figure 13: These are two results from a height sweep where the diameter was fixed at 2.5µm. The heights are given in the legend. These results were chosen because they illustrate the trend seen among all the results. There is a band of good blocking that shifts right with increased height. Along with this, the slope gets steeper, but the lower wavelengths transmit more.

The best single spectrum achieved had 3µm diameter and 2µm height. The average transmission from 1-6µm was 6.3% and the average transmission from 9-12µm was 91%.

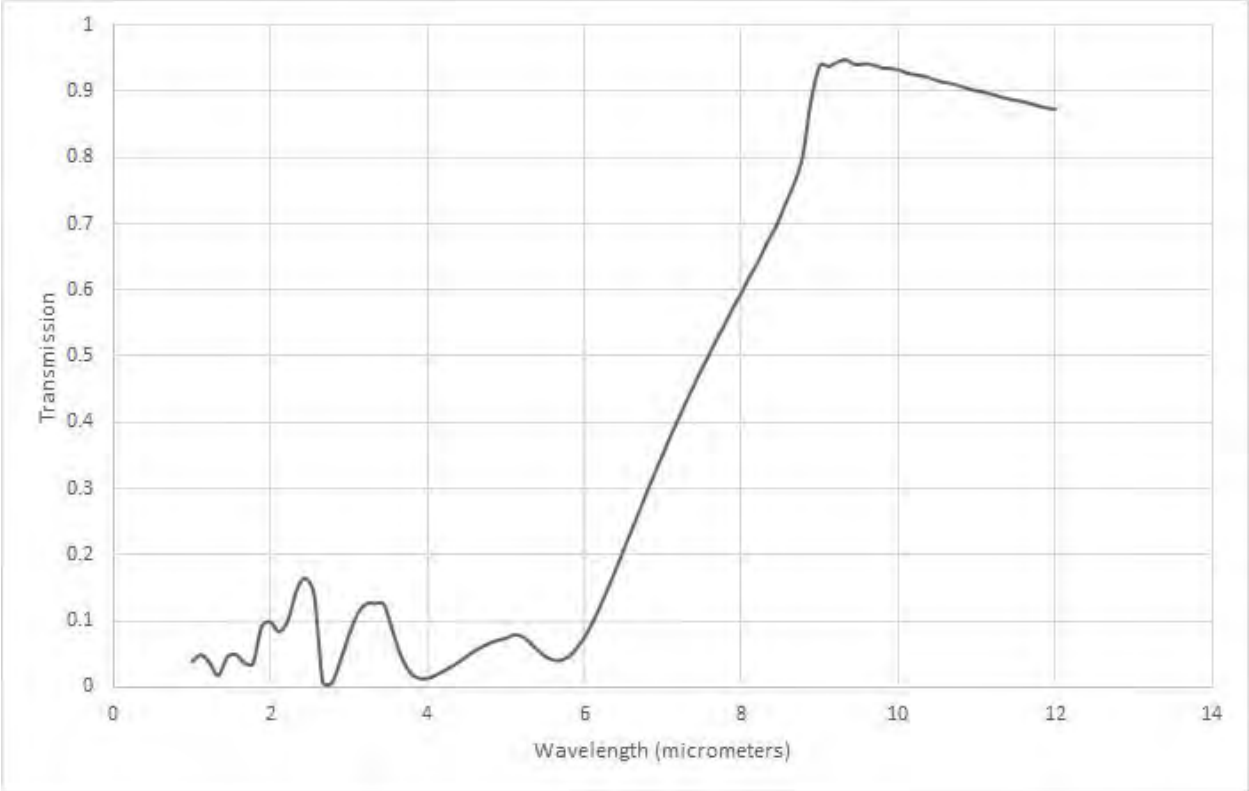

Figure 14: The best individual spectrum from a sweep.

It can be seen that it is very difficult to retain a steep slope while limiting leakage in the stopband. To reduce this effect, it is recommended to use multiple filters in succession to multiply the transmission spectra of the two designs.

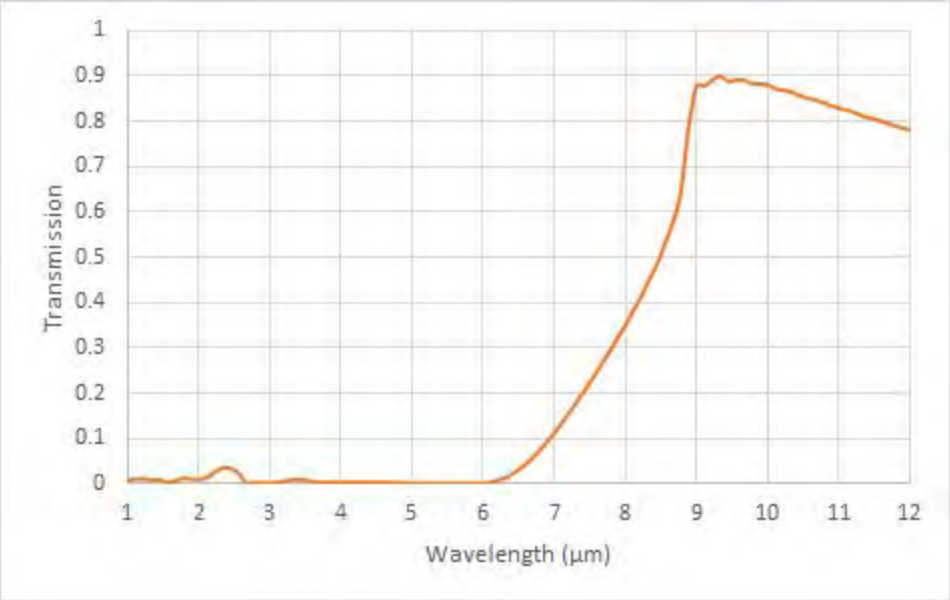

Figure 15: Example of a spectra made by combining two filters. Most of the undesired transmission in the stopband is reduced to under 0.5 % while the pass band is not as dramatically affected.

As exploration of cone array variations had converged on a single design, a manufacturing target was now established, and design exploration continued via testing of non-conic geometries and through development of an optimizer macro for Lumerical, which began with a series of randomized surfaces determined by a sum of sine waves of various frequencies and amplitudes, which the algorithm continued to vary and improve until optimal results were achieved.

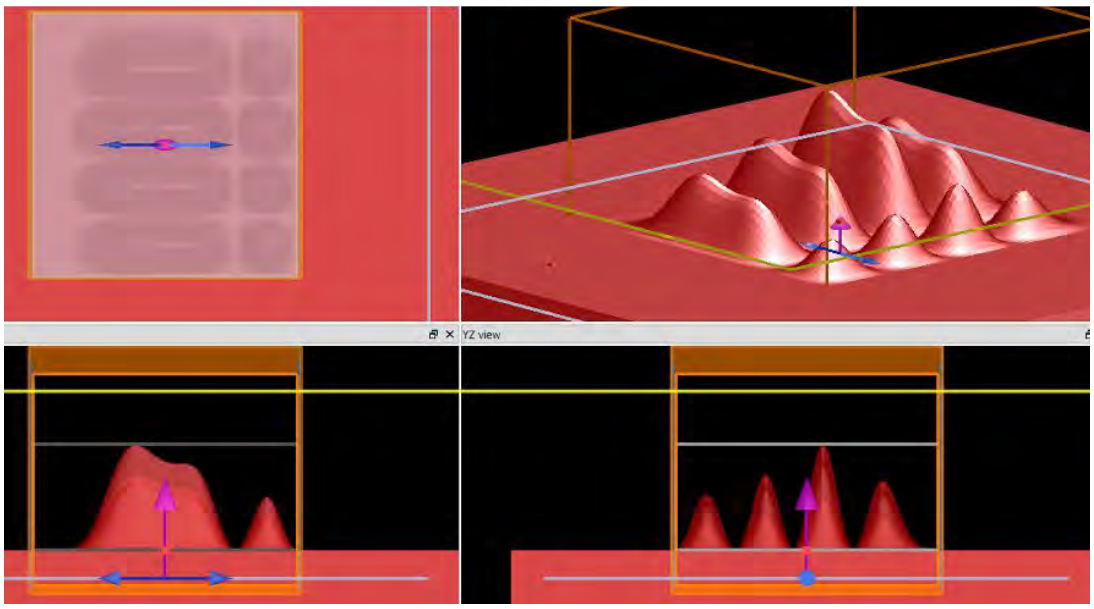

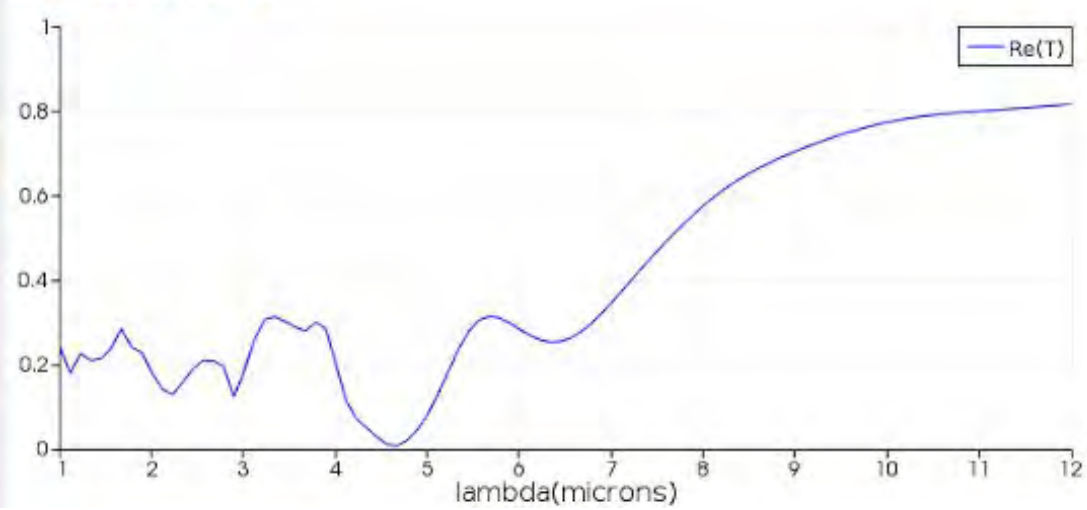

Figure 16: Initial results from optimi The trend goes in the right direction, but it's clearly not as good as other results. Nevertheless the results were encouraging, as they were different than anything previously produced..

The first optimizer macro used a very simple better/worse, yes/no algorithm. After researching other options, another type of algorithm was found that is probabilistic and less likely to get caught in local optima. However, it turns out that the old code was never actually that bad, since the new macro produces similar results. These are shown in figure 17.

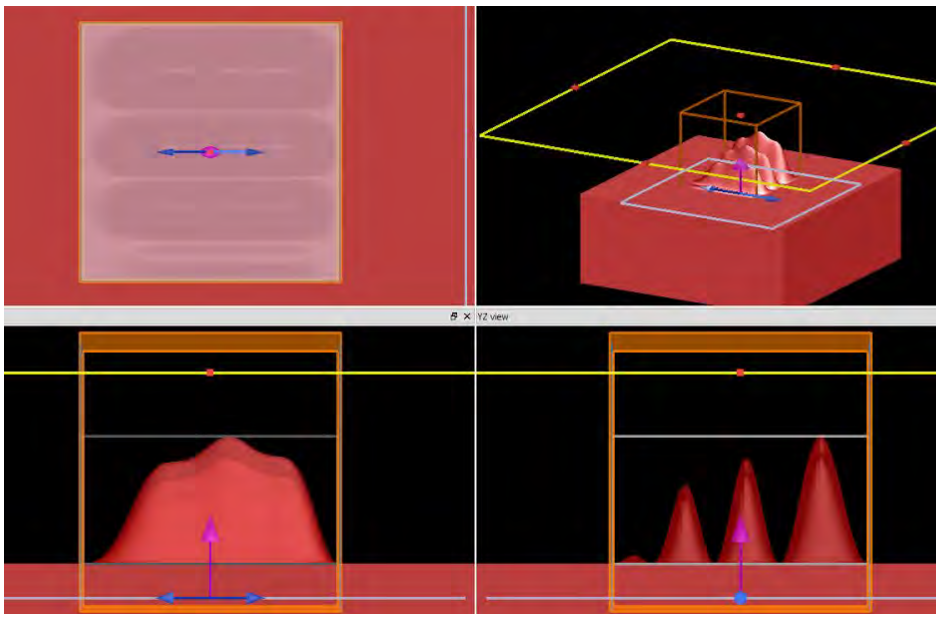

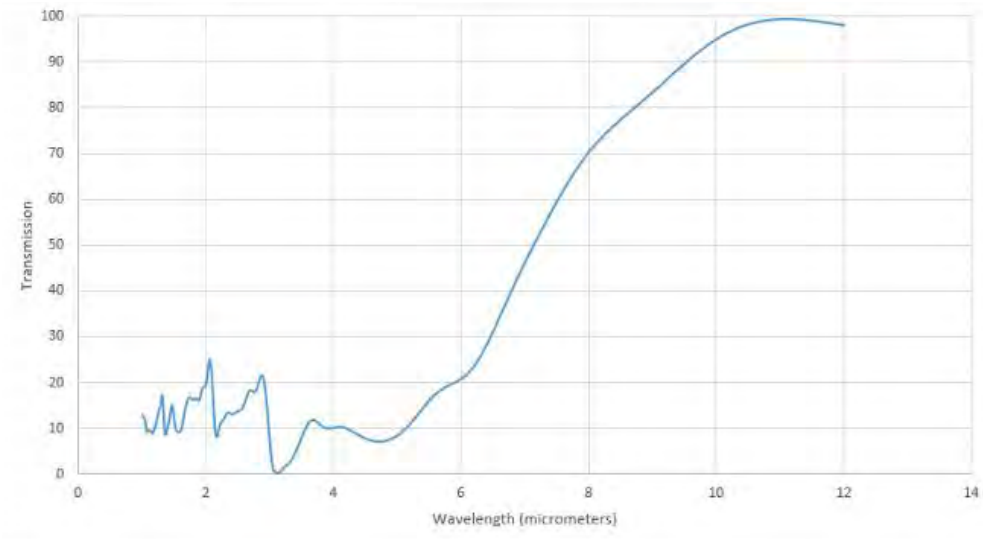

Figure 17: The result of the better optimization code. The results look very similar to the previous version, which is surprising. All results so far have given ridges parallel to the polarization angle.

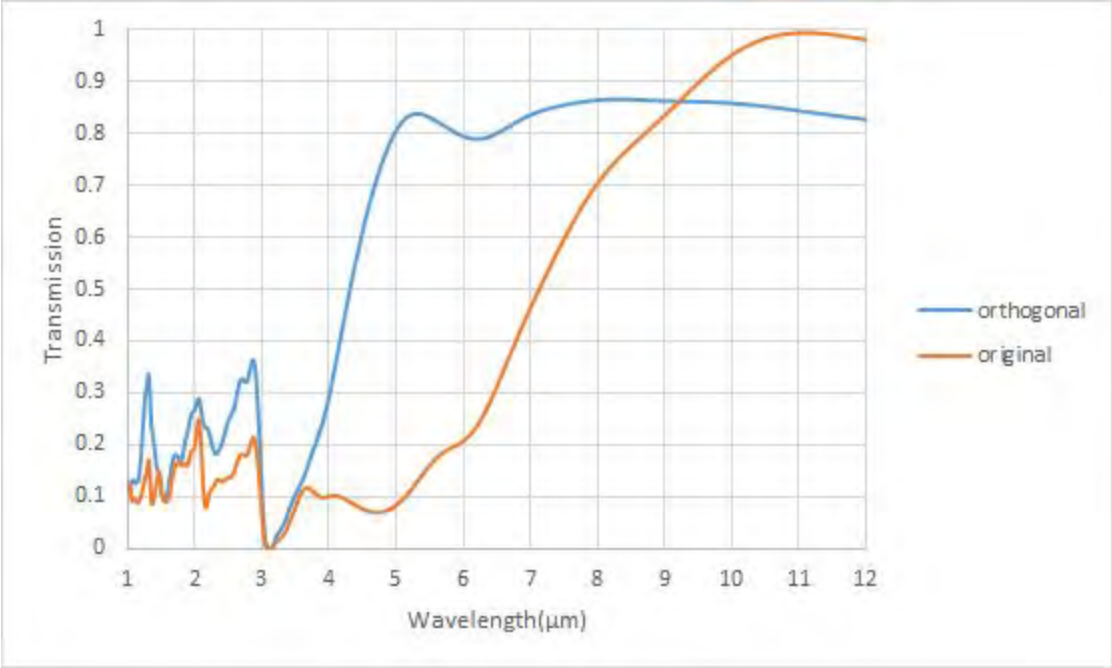

Figure 18: This graph of polarization dependence of the design in previous figure. The maximum difference is 72.9%. With further design, this could function as a polarizer.

RIE Etching

In attempting to manufacture the right circular cone design, the first place to look was in the manufacturing of black silicon. Black silicon is term for etched silicon on which small “microspikes” cause significant absorption at wavelengths less than the size of the microspikes. High absorption limits the transmission of these wavelengths, creating a transmission curve that can resemble a longpass filter. Prototypes described in reference literature where manufactured in part using a Deep Reactive Ion Etcher (DRIE). These spikes have comparable geometries to specifications determined in our FDTD simulations, and we had access to a Reactive Ion Etcher (RIE) through URNano, therefore we attempted to manufacture a proof of concept sample in house using the facilities and equipment available.

Figure 19: Image of the RIE setup in URNano cleanroom.

Reactive Ion Etching is a manufacturing process in which a mixture of gases is released into a vacuum chamber containing samples, where the gas is energized into plasma and accelerated at the sample by a radio frequency power source. In our initial attempts using the RIE, we relied on microscopic impurities that are not etched as quickly as the bare silicon to act as a spontaneous mask and hence a starting point for cone development. Initial RIE parameters and gas mixtures were referenced from a paper titled *Si-based Infrared Optical Filters* by Balcytis, Armandas, in which they

developed similar structures. The results from this paper are shown in the figure below. Further citation of this article is available in Appendix D.

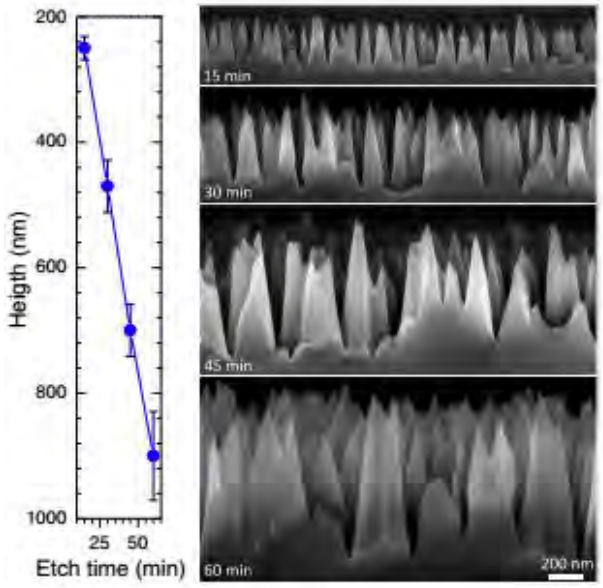

Fig. 1 The average height of b-Si spikes versus duration of reactive ion etching (RIE) and corresponding side-view SEM images (a common scale bar for all images).

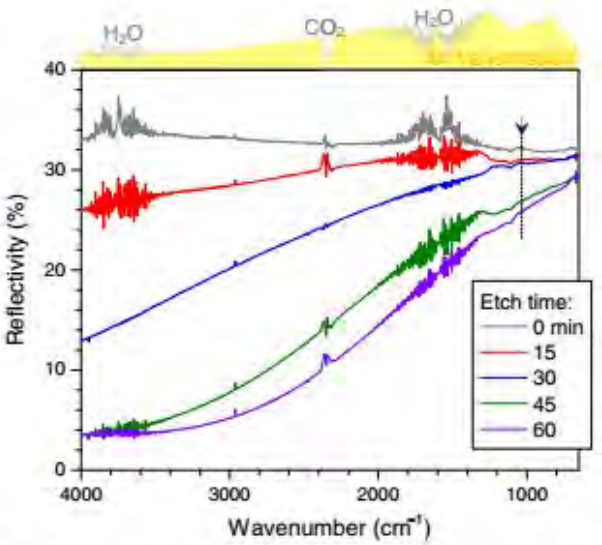

Fig. 2 IR reflectivity of b-Si for different heights of spikes, i.e., a different RIE duration (see Fig. 1). Most prominent background air transmission features are schematically shown on top of the plot to reveal the source of noise. Arrow shows the position of the second overtone of the transverse optical phonon mode of Si (1034 cm^{-1}).[19]

Figure 20: RIE Microspikes due to etch time and consequent transmission curves.

Forward Power	150 W
Pressure	150 mTorr
O_2/SF_6 Flow rate	45/35 sccm
Time	15 min - 2.5 hr

Figure 21: Initial RIE parameters used in sample manufacturing. Referenced from *Si-based Infrared Optical Filters.*

The initial results of these parameters on a untreated silicon wafer showed that there was no apparent etching that was occurring. After realizing this, the next step was to determine what was preventing the etcher from modifying the surface. We determined that the native oxide layer on the silicon wafer was acting as a mask. To remove this, we used a bath of 1% solution of hydrofluoric acid for 1 minute. After adding this preparatory step, the consequent results of the etching process showed a significant and noticeable change in reflection to the naked eye. The change of appearance became more noticeable with etch time. This gas mixture only showed effects in the center of the samples. When the gas mixture was adjusted to 25/35 O2/SF6, the visibly etched area spanned the entire sample.

Although the surface modification had noticeable effects on reflection in the visible spectrum, these results were not true for the infrared (See Metrology Section). Taking a look at the structures with electron microscopy, it was apparent that the spacing between structures was much farther than

the design, and the structures did not have a regular geometric shape. In addition, the height of the features were much smaller than the other paper had suggested for the same etcher parameters. The large spacing indicated that there might not be enough inhomogeneity across the surface to create the structures. In order to fix this, methods for applying different materials to the surface to cause the inhomogeneity intentionally and to not rely completely on the original properties of the surface.

One material that was used to attempt this was a solution of PMMA spin-coated on the surface for monolayer level thickness. This method however did not show any change in surface etching compared to the uncoated samples.

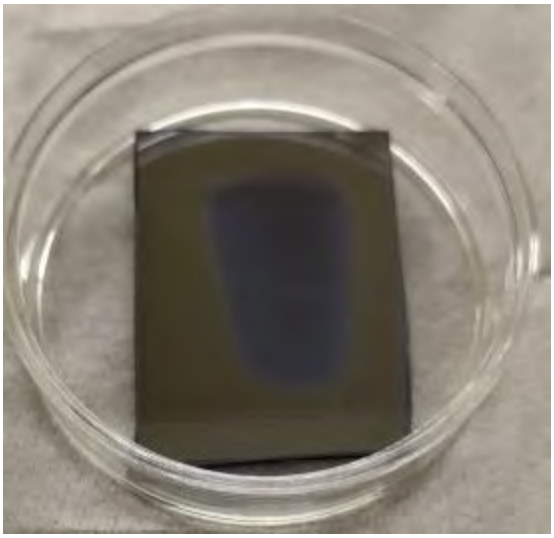

Figure 22: Image of S9, a sample that was treated with hydrofluoric acid to remove the native oxide and etched with the RIE. Most uncoated samples manufactured were similar in appearance to the depicted sample.

Polystyrene Bead Masking

After design simulations made clear that a controlled hexagonal array of cones was more effective than a randomized coverage by various sized cones, developing a method to appropriately mask and etch cones in this manner became a priority. Knowing that a close packed region of spheres creates a hexagonal array in two dimensions, we explored methods of depositing a close packed array of etchable spheres, with the idea that the anisotropic etching of the RIE would begin in exposed areas between spheres, then continue towards the center of each sphere as the spheres were etched away from the edges inward, until the beads are gone and a close packed array is formed, with each cone centered where a bead used to be. For such a mask, we needed a beads of the appropriate size made of a material that would etch at the correct rate relative to the silicon, and a method for depositing them in a close packed array. We settled on spin coating colloidal solution of polystyrene (latex) beads on samples which had been previously treated with a spin coat of Hexamethyldisilazane (HMDS), to create and then evaporate a uniform layer of HMDS to make the sample surface hydrophilic. This allowed the beads to hold to the surface as they were spun into a close packed formation.

Spin coating beads onto samples into a close packed array was successful, however due to the colloidal solutions only being 10wt% beads, the surface coverage of these close packed regions was initially only 5-10%. Our solution was to evaporate the solution on the samples before spin coating, using a hotplate set at 60°, adding drops of solution whenever the previously solution was significantly evaporated. This drastically improved surface area coverage, as will be later discussed in the Metrology section.

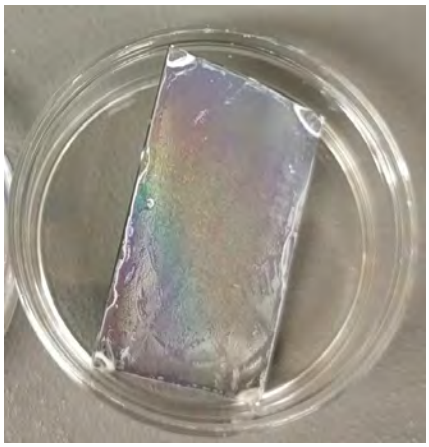

Figure 23: Image of S24, first sample to with significant close packing. Close packed samples have a visibly diffractive quality, as made apparent by the rainbow across the the sample.

KOH Wet etching with Polystyrene Beads

RIE etching of was not as effective at etching the silicon substrate as was hoped, however it did melt the polystyrene bead mask. This enabled us to use the previously unavailable approach of wet etching, in which the sample is bathed in a corrosive solution. Wet etches are isotropic, and as such a close packed array beads would not provide a substantial mask, as point contact to the substrate surface wouldn't restrict the surfaces for the solution to etch, and the beads would be easily dislodged once their single point of contact was corroded. Partially melted beads act as mask of close packed circles, which the solution etches around and eventually under to create pseudo-cones centered below the sphere remnants. This was the final etching process examined and shows promise for future development.

Metrology

Representative samples from each sample series have been measured in the FTIR main compartment, and have shown minimal departure in the infrared spectrum from unaltered silicon wafers, with the notable exception of sample S20. They were measured against a background containing no sample, in which case they all showed the standard silicon spectrum. A second series was done measuring the samples against a background of unaltered silicon to look for smaller differences between unaltered silicon and sample spectra, however this also showed no significant differences. Many samples had evidence of etching in the visible spectrum, therefore spectra were taken using a white light source to check if desirable high pass effect was present shifted in the visible. Visible spectra did not show a desired high pass response, but did show considerable variation, likely

due to the fact that most of the generated structures were on the order of several hundred nanometers or below, as seen in the following SEM images.

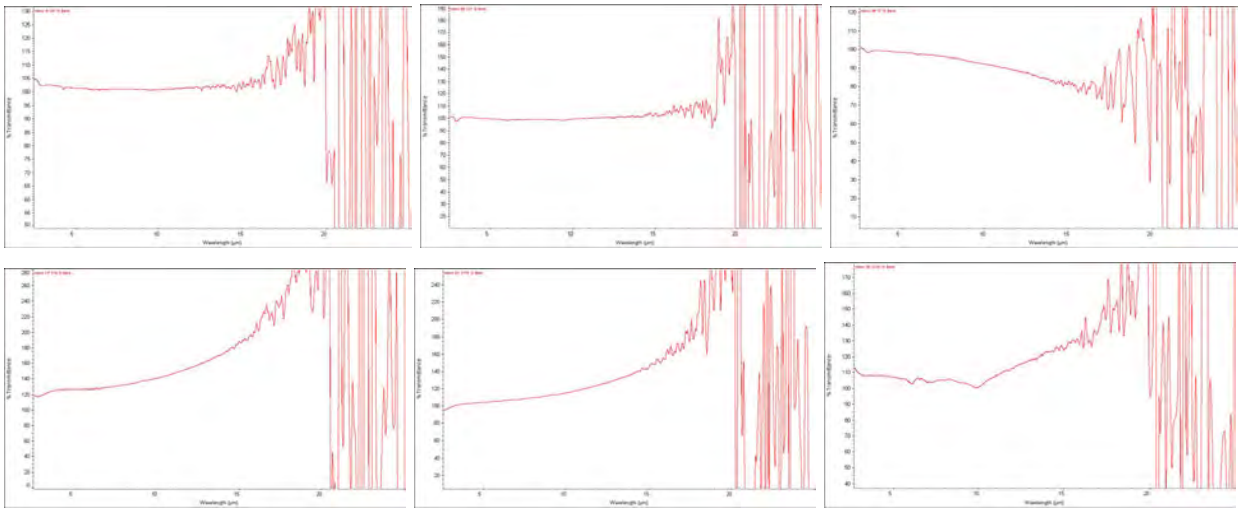

Figure 24: Comparison of various etched sample spectra on unaltered silicon wafer background. Left to right, top row shows samples S7, S21, S22, and bottom row shows samples S19, S17K, S13K.

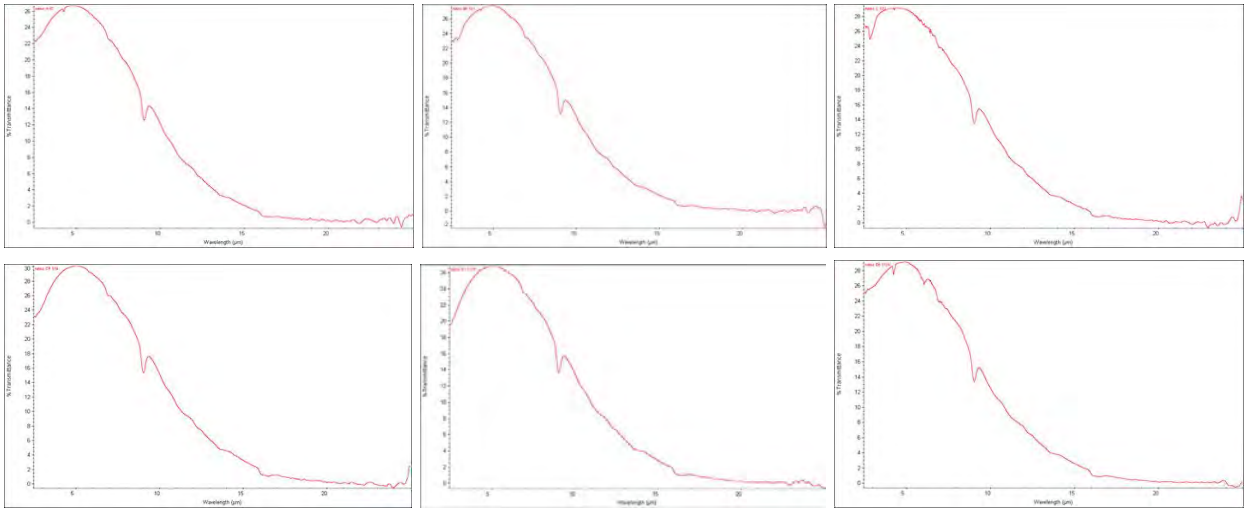

Figure 25: Comparison of various etched sample spectra with unblocked background. Left to right, top row shows samples S7, S21, S22, and bottom row shows samples S19, S17K, S13K.

Selected samples are representative of various processing series. These are representative of samples with latex beads, uncovered, and with PMMA as etched at 45/35 O2/SF6 % gas mixtures and 25/35 O2/SF6 % gas mixtures, and samples with latex beads removed by a plasma cleaning process known as ashing, in which the samples is barraged by oxygen plasma. The samples cleaned with an ashing process had been previously treated with a KOH wet etch, which will be discussed later. As we can see performance in the IR varies little from a bare silicon wafer, apparent even when a bare silicon wafer is used as a background. Spectra with a silicon wafer background are noisy after 18 µm, as total transmission in that range is below 2%, as seen in the spectra with an unblocked background,

therefore any change in transmission is drastically amplified. Description of each sample processing can be found in Appendix E.

Infrared spectra of sample S20 are abnormal in that S20 was completely non-transmissive to IR. S20, a sample which had light surface area coverage of 2µm beads with an RIE run time of 2 hours at a 43/35 % gas mixture, as far as we can tell had no unique change in process, as no one element of its process hasn't since been repeated on a different sample. It therefore seems unlikely that no one particular intentional manufacturing change is responsible for this unique behavior. We confirmed that it is not systematic error, so while the particular combination of manufacturing processes may be responsible, it seems more likely that an IR absorptive film may have formed on the sample. Such a film, however, did not appear on the Nomarski Microscope.

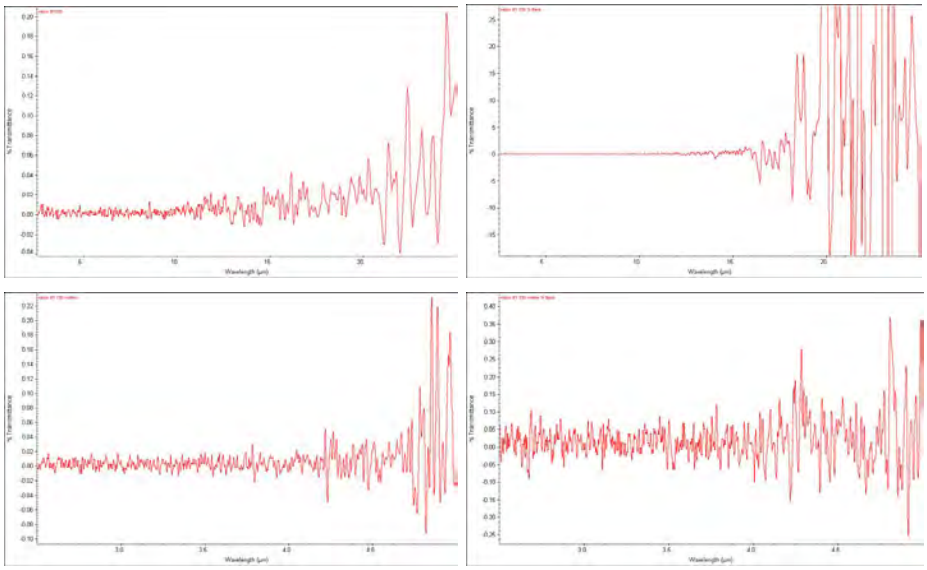

Figure 26: FTIR spectra of sample S20. Clockwise from top left:infrared spectrum, infrared using silicon wafer as background, visible using silicon wafer as background, visible. Graphs show noise centered on 0% transmission.

Integral to the successful etching of a controlled array of cones is the deposition of a close packed array of latex beads to act as a mask. Available colloidal bead solutions were 10 wt% beads, which was insufficient to achieve close packing across the sample, therefore the colloidal solution was evaporated on the sample to provide a higher concentration. The images below show the improvement in surface area coverage after solution evaporation was employed, as well as the surface residue intentionally left by the PMMA solution. Due to partial melting of the latex sphere in the RIE, we attempted a wet etching procedure using a 10 wt% potassium hydroxide (KOH) solution, where the surface area of melted latex acted as a mask. These images are also included below. These microscope images are colorful due to the use of Nomarski Microscopy, also known as Differential Interference Contrast Microscopy (DIC), in which a rotated prism is employed to change optical pathlength of sheared polarized beam paths, ultimately providing contrast along artifact edges.

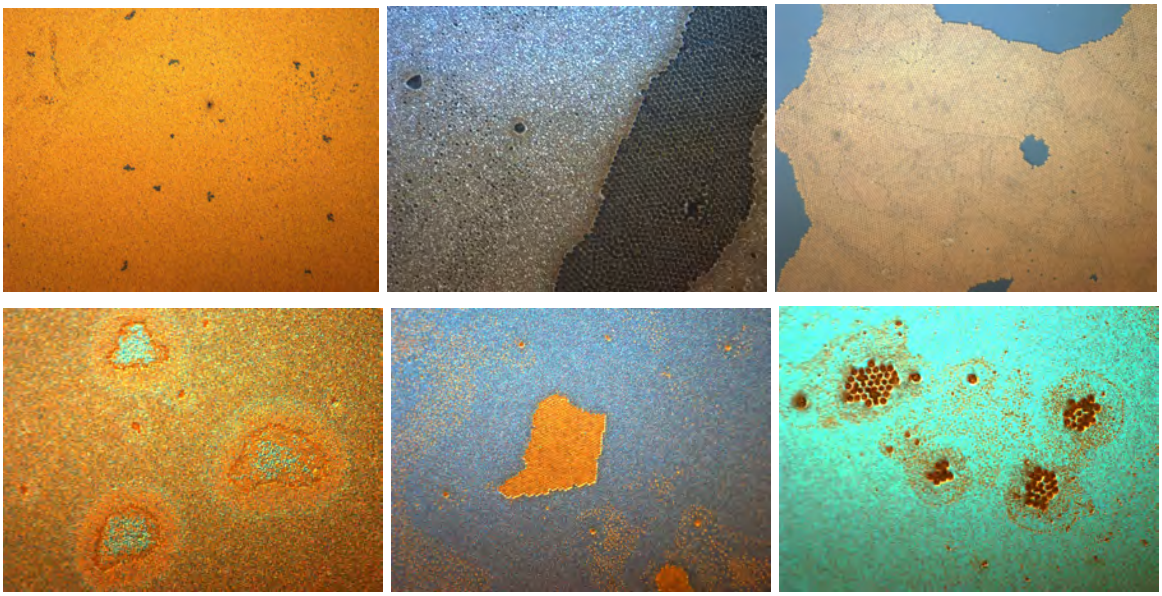

Figure 27: DIC Microscope images of close packed and KOT etched samples. Top row left to right: S9, S11, S23, samples showing PMMA and various levels of close packing surface coverage. Bottom row left to right: S13K, S17K, S18K. These are KOH etched samples showing significant etching in areas without beads, with varying effects on the beads themselves.

Representative samples of RIE etching series were imaged using a Scanning Electron Microscope (SEM). As seen in the images below, instead of considerable etching of the silicon and a controlled etching of the latex spheres until the spheres were removed from the surface as was our goal, the spheres instead partially melted, and the silicon, while visibly etched below the latex spheres, was only etched to a maximum of approximately 200nm. This process cannot be adjusted to minimize melting while still performing considerable etching of the silicon, as we found evidence of iron and nickel in spectra taken in conjunction with the SEM, which indicates that the longer RIE run times led to chamber ablation. Therefore, in order to prevent damage to the RIE, run times will be henceforth kept under three hours. Of the SEM imaged samples, S12 seems the most effective in etching uniformly towards the center of each ball, however the silicon wafer has not etched enough during the deterioration of the latex beads, and as mentioned previously, we are restricted from running higher forward power or long run times for preservation of the equipment.

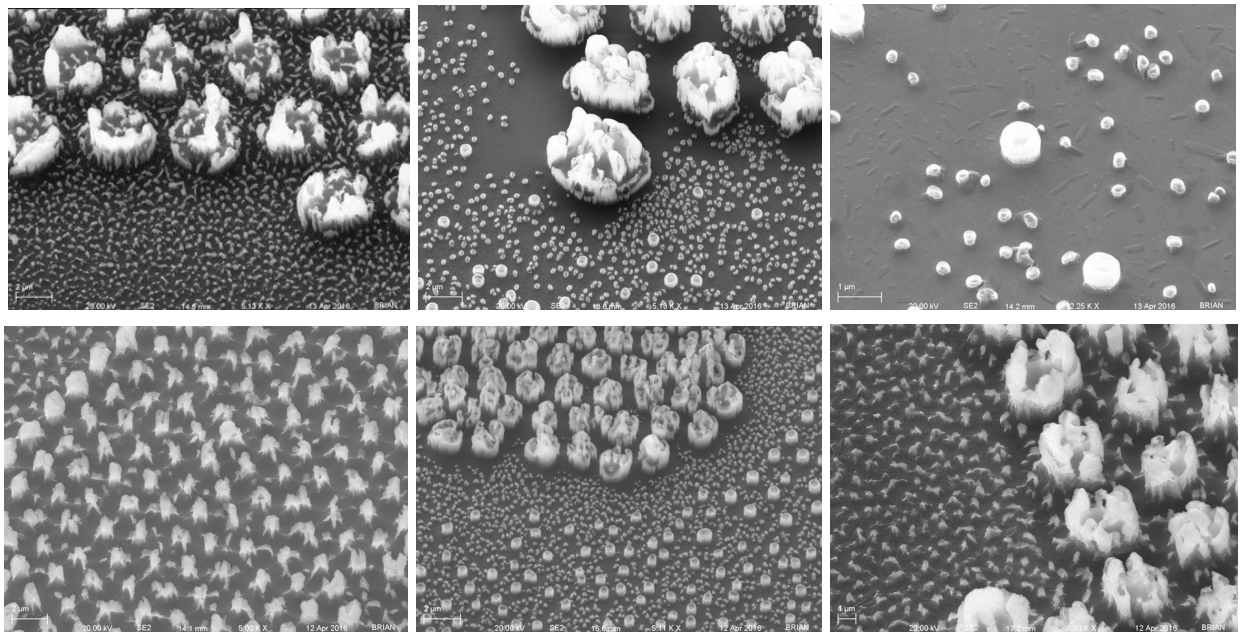

Figure 28: SEM images of latex bead and PMMA samples etched in the RIE. Top, left to right: S14, S18, S19. Bottom, left to right: S12, S17, S13. S19 was coated in PMMA solution, whereas all others had either 2 or 5µm beads.

The series of images below document our attempts at achieving a uniform distribution of surface structures before we began employing latex beads as an etching mask. As can be seen in the images below, we achieved a uniform distribution of structures without a mask, but they didn't have the desired conic profile, and it seems that our previous gas mixture of 45%/35% O2/SF6 resulted in a redeposition of evaporated silicon. As can been seen in S14 and S19 above, this became less of an issue after altering our gas mixture to 25/35% O2/SF6.

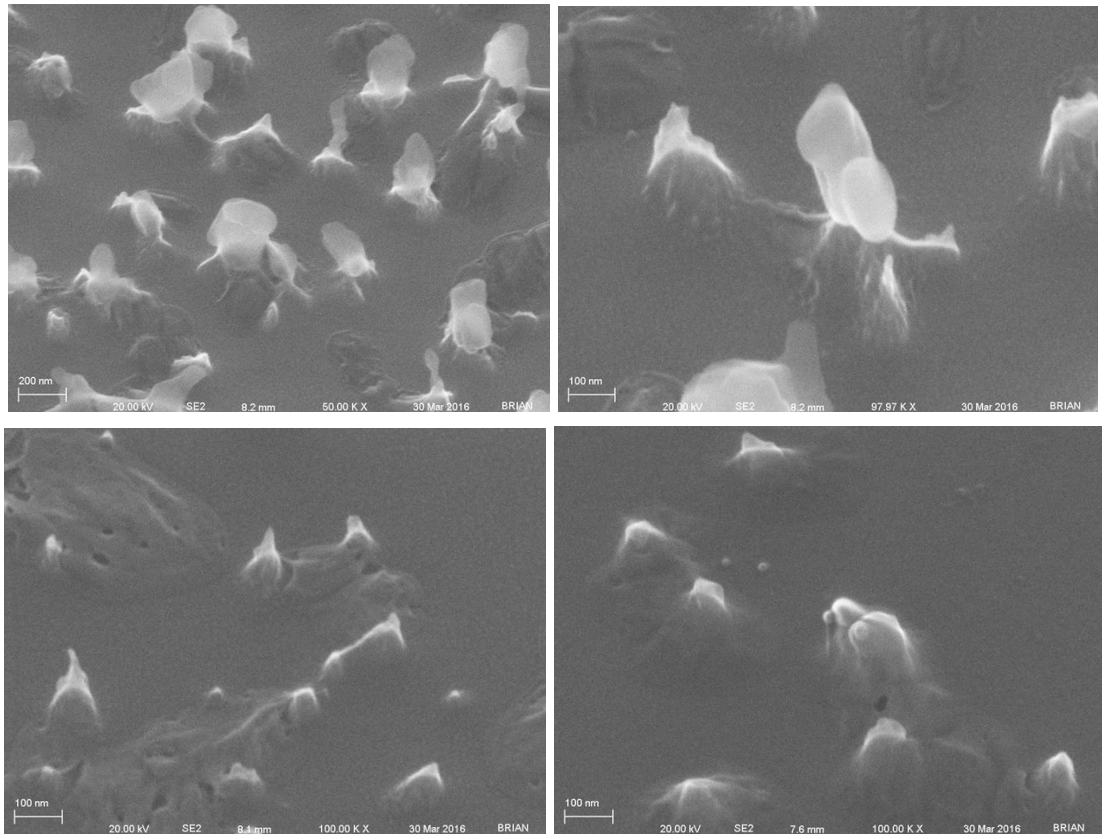

Figure 29: SEM images of samples S7-S9. Clockwise from top left: S7 at 50K, 97.97K, S8 at 100K, S9 at 100K. Scale is available in bottom left corner of each image. Artifacts in S7 seem to be semi-regular pillars, often with considerable necking, resulting in a shape resembling mounds topped with large particulates. Artifacts in S8 and S9 are more similar to mounds without necking.

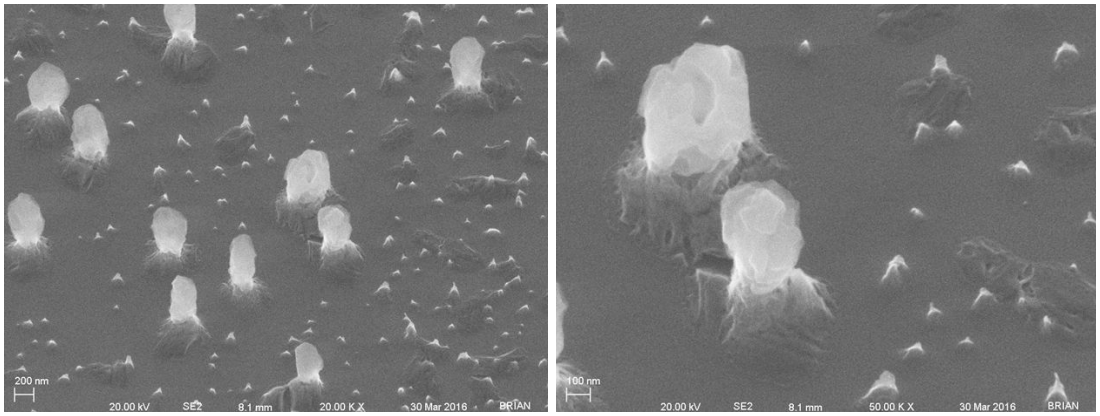

Figure 30: SEM images of sample S8. Magnification for left image is 5K, 20K for right. Scale is available in bottom left corner of each image. Larger particulates seem to be evaporated silicon redeposited on the surface.

The following images show the effects of KOH wet etching on samples previously etched with the RIE. As we can see, etching in areas without beads creates a porous surface without individual structures, whereas in regions with close packed beads we see continued

etching of pillars or cones below the remnants of latex beads. Similar minimal pillar formation below beads was previously observed in samples etched with the RIE, however the addition of wet etching seems to have enhanced the effect, albeit incrementally.

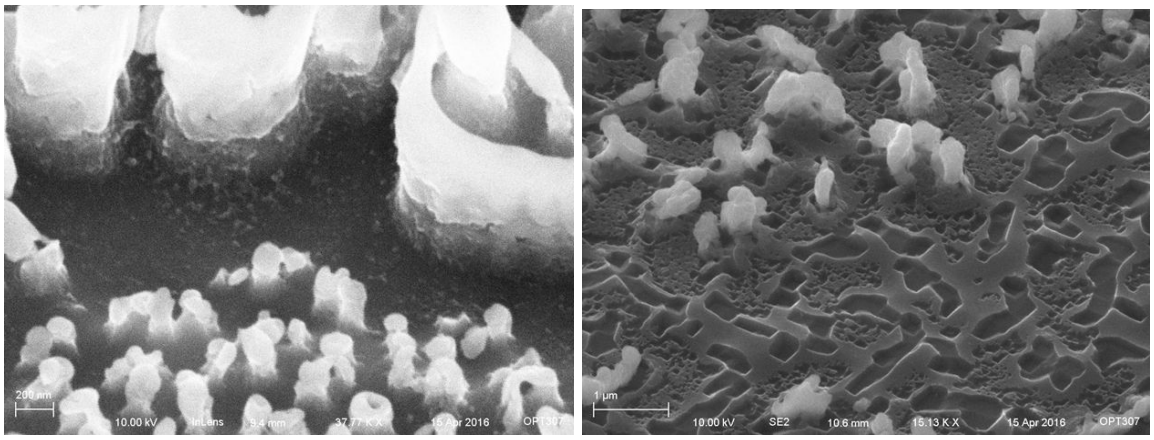

Figure 31: SEM images of samples S12K on left and S13K on right. Incremental pillar formation under beads visible on S12K, and induced porosity visible in areas without beads on S13K.

Following samples were produced using a hot plate to partially melt the polystyrene beads instead of RIE etching, however during wet etching, the melted bead mask often peeled off earlier than desired, therefore not producing a masking effect for an adequate period.

Risk Assessment

Thin film coatings and microstructures are often very sensitive to incident angle variation and polarization, therefore it is desirable that a final product be angularly toleranced so that it doesn't fail due to minute angular misalignment. While polarization tolerancing is also desirable, characterization of performance with polarization in this case is sufficient, as depending on the application, the source may have some level of polarization that the filter must be matched with.

The primary cause of catastrophic coating failure is mismatched thermal expansion, which can cause a coating to split off from a substrate, shatter the coating, or break the substrate. As our designs employ etching of structures directly on the substrate, catastrophic failure is not a necessary consideration, therefore in this matter etched substrate designs have a considerable advantage over conventional thin film coatings. While thermal expansion does inherently affect the size and spacing of surface structures, as the volume of the structures themselves is minute, change in performance due to thermal expansion is likely to be negligible.

In the case of high power laser applications, it is important to map the electric field intensity throughout a coating to prevent maxima that may 'blow up' said coating. As no power specifications have been given and usage of such a filter in an infrared laser is unlikely, this is not a major concern in our design. If, however, further designs are created for such applications using our design study, electric field evaluation and further simulations are strongly recommended to prevent melting or distortion or surface structures.

Transition Plans

All Lumerical design files, FTIR spectra, and manufacturing images will be saved on a flash drive and sent to the customer, along with the lab notebooks where procedures and notes were recorded. This will enable the customer to continue the work performed, or even pass the project on to a future senior design team.

Appendix A

General overview of plasmonic simulations:

The software we use takes Maxwell's equations and evaluates them at every point in space through brute force. The FDTD software has a lot of options of how to run it, so this is just a general overview of the settings I've chosen for our simulations. For the actual simulation area, I use a mesh step of 1nm, a mesh accuracy of 3, I use staircasing for interfaces, and for most other things I use the default settings. For the source, I'm using a standard plane wave of 1-12µm, not optimized for short pulse. To create the holes, I put in an array of cylinders with an index of 1, defined as a dielectric. I give the cylinders a mesh order of 2 and everything else is 3. For the monitor, use a frequency domain field and power monitor. I only measure output power and the standard Fourier transform. I measure 20 points in the spectrum and I use a linear wavelength spacing.

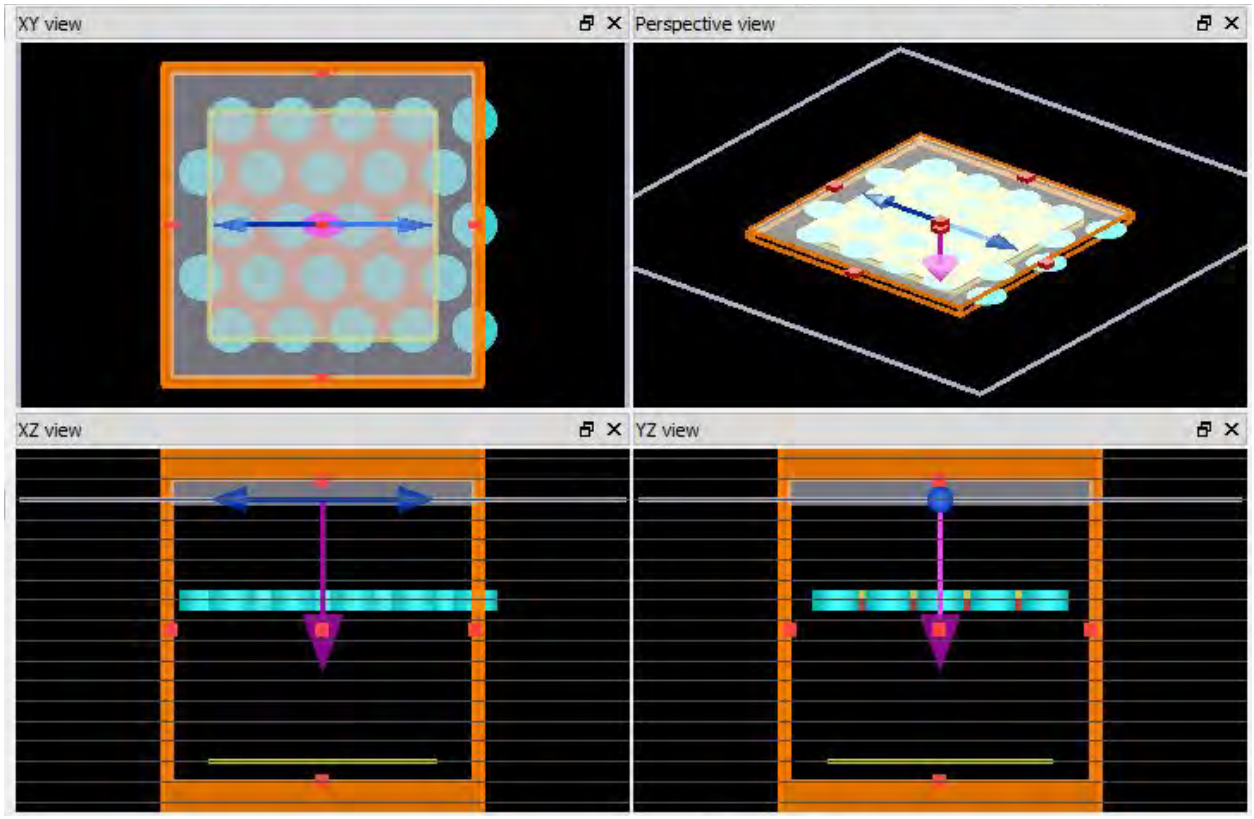

General Overview of etched silicon simulations:

For the FDTD, I use a staircase mesh because there aren't and dielectric-metal interfaces. Also, there is a limit to manufacturing resolution which makes more accurate simulations pointless. I

continue to use a mesh accuracy of 3 and minimum mesh size of 1nm, because anything smaller would be insignificant when the smallest wavelength is 1µm. These parameters can be made more accurate if we find a design that we really like and want very good data for. FDTD boundary conditions are periodic in x and y, and perfect absorbers in +/- z. The periodic boundaries give an effectively infinite array simulation. The source is a 1-12µm plane wave, with all other settings on default. The monitor records 100 linearly spaced wavelength points, standard fourier transform, and output power.

Appendix B

Project Schedule and History:

fall semester:

December-

~~Get comfortable with design software.~~

~~Meet with Vamivakas and McIntyre to figure out manufacturing capabilities.~~

spring semester:

January-

~~Focus on getting the one specific spectrum asked for.~~

~~Get access to all materials and modes of manufacturing we will need.~~

February-

~~Start expanding from one design to try and find the variables that affect performance~~

~~Schedule time on the necessary fab/metrology equipment~~

March-

~~Continue figuring out design parameters that are relevant~~

~~Start producing proof of concept filters~~

~~Figure out manufacturing tolerances on relevant design parameters~~

Tweak designs based on measured vs. expected results and fabrication limitations

April-

Continue design study, expand to other types of filters if possible

Produce final filters

~~Take all necessary pictures and measurements~~

~~Put together final presentation~~

~~Present to school and Materion~~

Appendix C

Plasmonics Math:

Our Conventional model for diffraction through an aperture follows the Fraunhofer (Far-Field) approximation.

$$I(\theta) \simeq I_0 \frac{(kr)^2}{4\pi} \left| \frac{2J_1(kr\sin\theta)}{kr\sin\theta} \right|^2$$

However, for sub-wavelength apertures utilizing a dielectric to metal interface, this approximation no longer holds true in a couple of its assumptions. The main reason this model is no longer accurate is that it doesn't take into account the local surface plasmons generated at the aperture. This affects the field in the image plane.

Drude model for free electrons in metal:

$$\varepsilon_m = 1 - \frac{\omega_P{}^2}{\omega(\omega + i\gamma)}$$

This models the transport properties for free electrons in metals. In high frequencies (wp < w) dielectric constant in metals is positive, which give rise to dispersion modes governed by:

$$\omega^2 = \omega_p{}^2 + c^2k^2$$

These modes are known as Bulk Plasmon Polaritons (BPPs) and are a result of the coupling of incident light with the free electrons in the metal.

When wp > w: light cannot propagate due to the negative permittivity of metal. However, When the surface of a noble metal is interfaced with a dielectric, light causes evanescent modes, which yields oscillating waves on the surface of the metal. These waves are known as surface plasmon polaritons. (SPPs)

Dispersion modes:

$$k_{SPP} = \frac{\omega}{c}\sqrt{\frac{\varepsilon_m\varepsilon_d}{\varepsilon_m + \varepsilon_d}} \qquad \omega < \omega_{SP} \equiv \omega_P/\sqrt{1+\varepsilon_d} \quad \varepsilon_m + \varepsilon_d < 0$$

- For propagation to occur Ksp must be real.
- Only way to get more modes is to have magnetic material.

- Ratio of Electric field components with respect to direction of propagation
  - Inside the dielectric: $(E_\perp/E_{//})_d = \sqrt{\varepsilon_m/\varepsilon_d}$
  - Inside the metal: $(E_\perp/E_{//})_m = -\sqrt{\varepsilon_d/\varepsilon_m}$

- Propagation Length of SPP at interface $L_{SPP} \approx \varepsilon_m'^{\,2}/k_0\varepsilon_m''\varepsilon_d^{3/2}$
  - ε ' and ε " are the real and imaginary parts of metal permittivity.
- Decay Length
  - Dielectric side: $\delta_d \approx \sqrt{|\varepsilon_m'|}/k_0\varepsilon_d$
  - Metal side: $\delta_m \approx 1/k_0\sqrt{|\varepsilon_m'|}$
    - Higher confinement in metal side.

These surface modes enhance field amplitudes above apertures to compensate for attenuation in the non propagating aperture.

Assume a sheet of metal infinitely thin, with perfect conductivity. Bethe found it behaves as a dipole.

- For circular apertures
  - Cutoff wavelength is approximately D < Lambda/2.
- Transmission Coefficient for incident plane wave

$$T = \frac{64}{27\pi^2}(kr)^4.$$

- Bethe-Bouwkamp Analysis:

*To account for thicknesses, must incorporate numerical simulations.

Beaming Phenomenon:

When periodic corrugations are placed on the entrance AND exit surfaces, scattering and interference in and out of the plane gives rise to a beaming effect.

  - This effect is optimized when the modes of both the periodic structures and grooves match in frequency.

Appendix D

Balcytis, Armandas. "Si-based Infrared Optical Filters." *SPIE Digital Library*. SPIE, 14 Dec. 2015. Web. 25 Feb. 2016.

Appendix E

Sample Descriptions:

All samples underwent an HF strip and P.20 spin coat prior to other processing unless otherwise noted

S1 PMMA spin coat 950w, 1:20 hr etching in RIE with 35% SF6/45% O2 at 150mT

S2 HF strip, 1um diameter feature, 2000RPM spin coat

S3 HF strip

S4 untreated

S5 1um diameter latex spin coat at 2000 RPM w/o HF strip

S6 35% SF6/ 45%O2, 150w, 0:20hr etch

S7 HF strip, 1:30 hr etching in RIE with 35%O2/45%SF6

S8 PMMA spin coat, FP 150w, HF strip 1/100 120s, 1:30 hr etching RIE 35%O2/45%SF6

S9 PMMa spin coat, FP 150w, HF strip 1/100 120s, 1:30 hr etching RIE 35%O2/ 45%SF6

S10 35 O2/45 SF6, at 150w for 1:30hr

S11 P.20 at 2000rpm for 60s, 2um latex beads at 2000rpm for 60s, RIE at 25/35 at 160w for 2hr

S12 P.20 at 2000 rpm for 60s, 2um latex beads at 2000rpm for 60s, RIE 25/35 at 160w for 1hr, then 100w for 1.5hr

S12K S12, followed by 10 min KOH wet etch in 10% soln and ashing

S13 P.20 at 2000rpm for 60s, 5um latex beads at 2000rpm for 60s, RIE 25/35 at 160w for 1hr, then 100w for 2.5hr

S13K S13, followed by 10 min KOH wet etch in 10% soln and ashing

S14 P.20 at 2000rpm for 60s, 5um latex beads at 20000rpm for 60sw, RIE 25/35 at 160w for 2hr

S15 2um latex bead spin coat 2000rpm/60s, no etch

S16 P.20 2000rpm for 60s, 5um latex beads at 2000rpm for 60s, repeat with 500 rpm for 60s, no etch

S17 1um latex bead spin coat, RIE 25/35 at 150w for 1.5 hr

S17K S17, followed by 10 min KOH wet etch in 10% soln and ashing

S18 5um latex bead spin coat, RIE 25/35 at 150w for 1.5hr

S18K S18, followed by 10 min KOH wet etch in 10% soln and ashing

S19 PMMA 1500 rpm spin coat, RIE forward power 150w, 25/35 for 1.5hr

S20 1um latex bead 1000 rpm spin coat, RIE at 45/35 O2/SF6 for 2hr

S21 6um latex bead 1500 rpm spin coat, RIE at 45/35 O2/SF6 for 2hr

S22 Plain wafer, RIE forward power 150w, 25/35 for 1.5hr

S23 2um latex bead evaporation at 60°C: 2 drop, wait 30s x4 w/ spreading during heat, spin 1000rpm/60s

S24 2um latex bead evaporation at 60°C: 2 drop, wait 120s x3, spin coat 2000rpm/ 60s

Appendix F

Design ideas that were tried and abandoned.

Gold coated TEM windows:

Our original design concept focused on engineering the plasmonic effects of gold coated silicon nitride TEM windows. This concept was abandoned after the customer requested designs that did not use metals at all, and preferably only etched silicon substrates.

Attempts to measure the TEM window filters in the main compartment have proven unsuccessful as seen in Figure 22, because not enough light passed through the filter onto the detector as compared to the unexposed detector area. The unexposed portion of the detector was detecting noise in the same manner as the entire detector when we measured the fully blocked aperture. This can be addressed by either ensuring that more of the detector receives a signal from TEM window filters, or by using an apparatus where the TEM window nanoarray fills a significant portion of the detector.

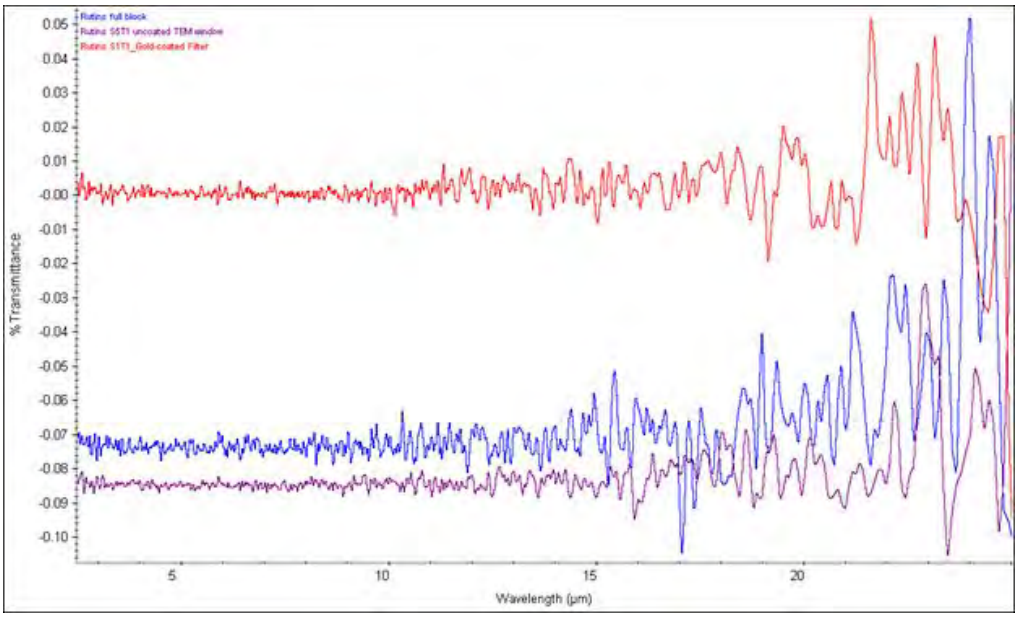

Figure 22: Spectra of uncoated and gold coated TEM windows measured with the main compartment of the FTIR, as compared with the measured spectrum of a fully blocked aperture. All three spectra are very similar, implying that not enough light passed through the TEM window aperture to produce a discernable signal. Axes are transmission % with respect to wavelength in micrometers. The red signal is from the gold coated window, purple is from the uncoated window, and red is the full block.

In measuring the spectra of KBr slides, we found that KBr is quite transparent across the infrared. This may allow us to use KBr slides as a film on which to assemble a hexagonal array of TEM

window filters. This has it's own disadvantages, as the majority of the aperture area will be covered by the TEM window substrate as opposed to actual nanoarray area, and there are transparent areas between the TEM windows. We are currently employing the second approach of imaging the TEM window nanoarray across an entire detector using the FTIR microscope attachment. It can measure both in reflection and transmission, and the nanoarray almost fills the entire aperture and is imaged onto most of the detector. Attempts at using the FTIR microscope in a somewhat conventional manner have so far proven unsuccessful. This may have to do with how the background is subtracted from the signal. We have therefore opted to manually calculate the signal by removing the background noise and normalizing with transmission. This approach has also not produced accurate results, as there are cases of negative transmission values, however this approach seems to show promise, and we expect to get accurate results from the FTIR in short order.The approach of manual background subtraction did not resolve our issues in in collecting plasmonic design spectra.

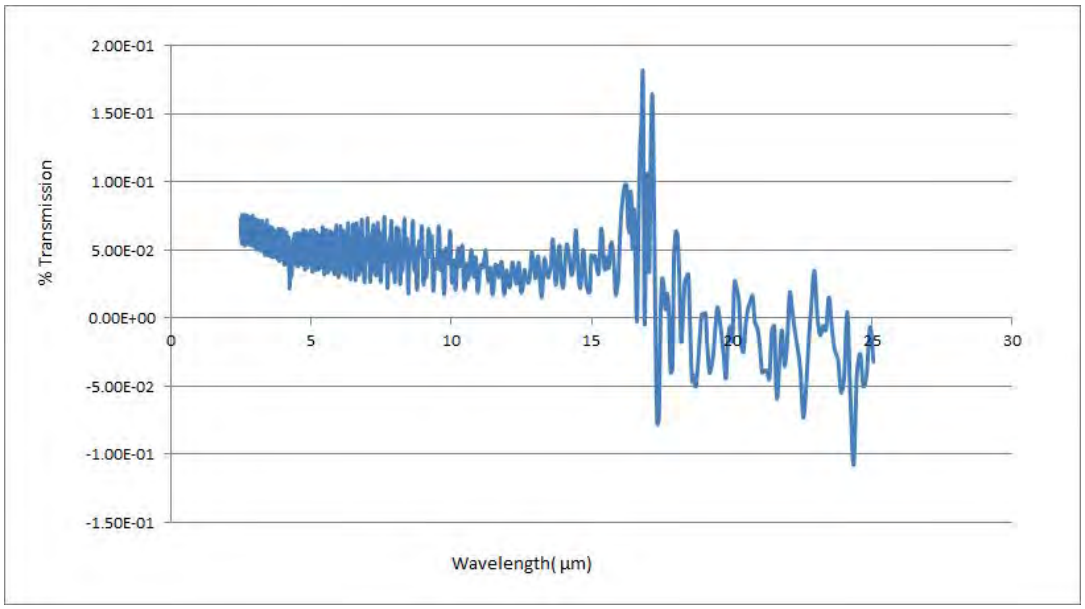

Figure 23: Manually calculated transmission through gold-coated filter with respect to wavelength. Calculated using equation:(Signal-Noise)/(Full Transmission-Noise).

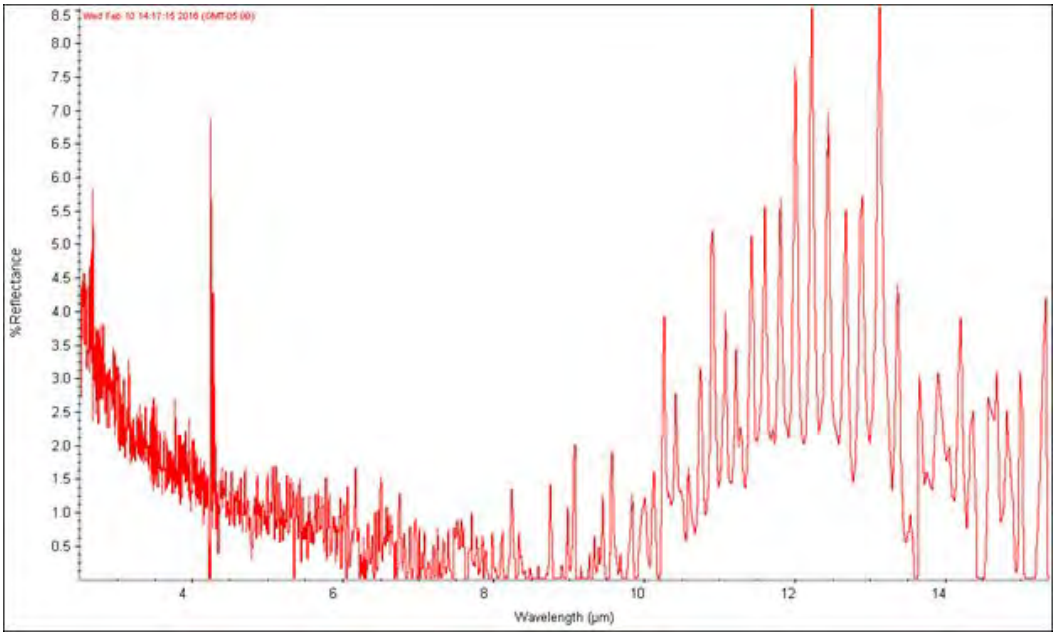

Figure 24: Reflection spectrum of gold coated filter using the FTIR microscope attachment. Some signal is visible here, however it is noisy. Unfortunately we cannot confidently say that this spectrum is accurate. Axes are transmission % with respect to wavelength in micrometers.

Varied Size Scattering:

Artifacts doped into a material or etched on a substrate surface tend to scatter only wavelengths on their order of magnitude and below. By creating an array of scattering artifacts of varying sizes smaller than 8µm, we can scatter the undesired spectrum away from the beam path. Some of the undesired spectrum may scatter close to the angle of the desired spectrum, but with enough distance from the filter the majority of this shouldn't be visible along the beam path. The simulations below have not yet been run, as we are currently prioritizing simulation of the black silicon and angular filtering designs.

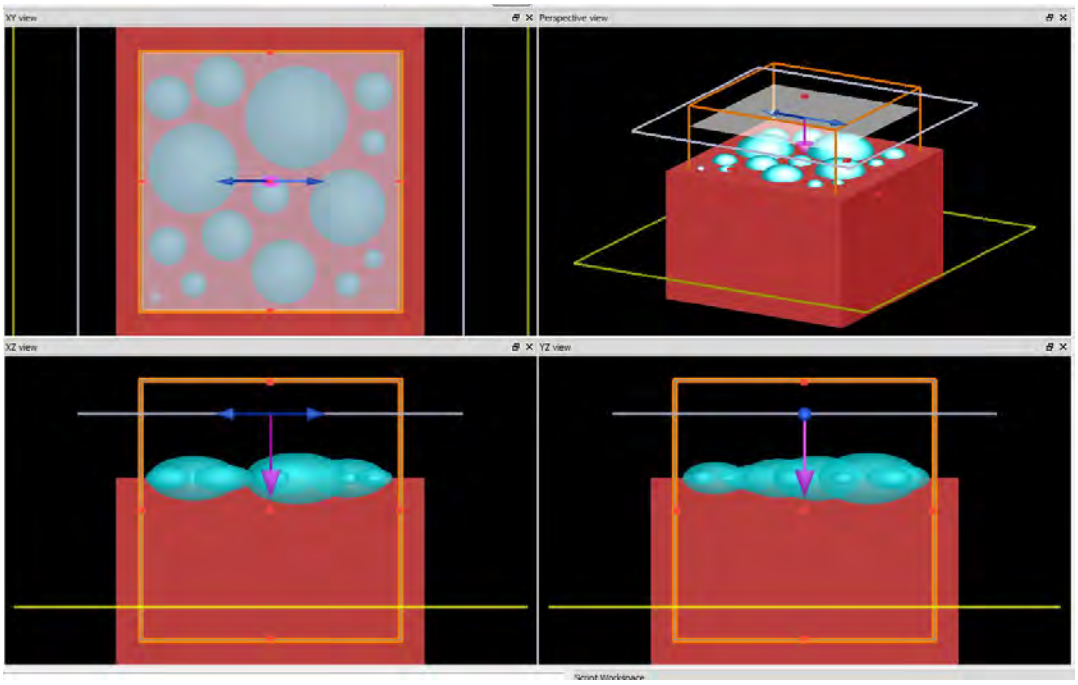

Figure 16: Lumerical model of Varied Size Scattering design. Blue spheres are 'etched' material, meaning that in this case the artifacts will be concave into the silicon, however the material of these spheres can easily be changed to repurpose the design for convex artifacts.

Angular Filtering:

The principle of this design idea is that both sides of the substrate are textured, and the structures work together to produce filtering. On the entrance side, the light passes through a simple line pair grating. This distributes the wavelengths within the substrate angularly. The angle of each wavelength can be easily calculated, which is what leads to the second structure. The structure on the back surface refracts the undesired portion of the spectrum out of the beam path while minimally affecting the desired spectrum of 8-12µm. The back surface design relies on the principle that light with a wider incident angle will only reach a given depth within a periodic well structure, while smaller incident angle will reach all of the structure. Regions that receive none of the desired spectrum will refract the undesired spectrum out of the beam path. Key issues with this concept are output power, as certain microlenses in the periodic structure may obstruct the recollimation of the desired spectrum. Depending on the grating line pair period and the period of the back surface structures, the line pairs may not appear as point sources at the back surface, or a given period may receive light from too many point sources and fail to correctly collimate.

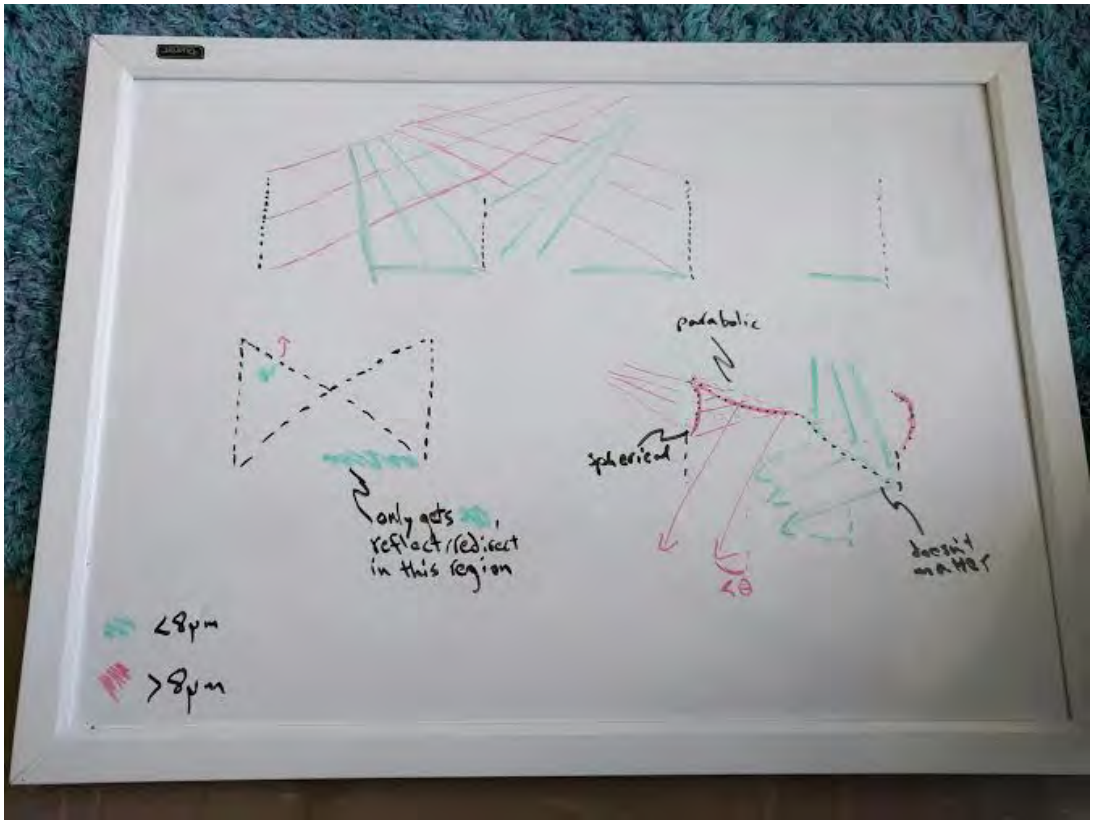

Figure 17: Crude diagram of the angular filtering design idea. Periodic array of microlenses may recollimate desired spectrum and refract away undesired portion of spectrum.

Grating-Microlens:

Similar to the Angular Filtering design, the we can employ a regular array of spherical microlenses that on the back surface of a substrate to select a particular wavelength to create a notch filter or low pass edge filter. Microlens curvature can be chosen to match a particular incident cone angle which corresponds given wavelengths, while wavelengths outside of the desired cone angle will not be collimated and therefore not be visible in the far field. Like the angular filter design concept, this design is also limited by whether or not the line pairs in the front surface grating appear as point sources, and if the can be etched to align with the microlens array.

Grating - TIR

Again, the principle of this design idea is that both sides of the substrate are textured, and the structures work together to produce filtering. On the entrance side, the light passes through a simple line pair grating. This distributes the wavelengths within the substrate angularly. The angle of each wavelength can be easily calculated, which is what leads to the second structure. On the back side, the substrate is etched with steep spikes that run the length of the substrate parallel to the grating lines. The angle of the spikes is chosen to produce total internal reflection for all wavelengths below the desired filter cutoff wavelength, and to pass all wavelengths above this cutoff. Achieving TIR in a silicon-air interface doesn't require extreme angles because of the large index difference at the interface. This system is diagrammed in figure 16. Potential issues with this design are that the lower

wavelengths might not continue to be trapped after the first couple bounces, and that the E-field could build up enormously within the spikes if all the light is trapped there.

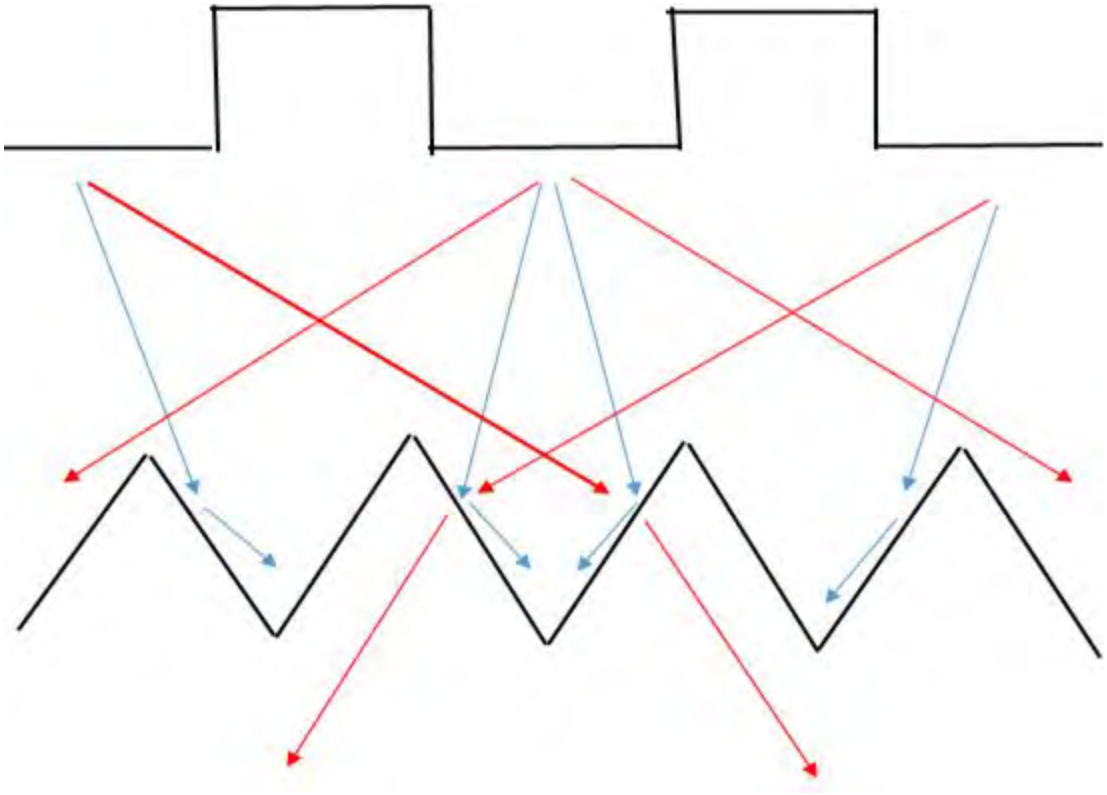

Figure 18: Grating-TIR design of an optical filter. The shorter wavelengths get trapped by TIR and the longer wavelengths refract out.